



**HAL**  
open science

**Effect of deposition reactive gas ratio, RF power and substrate temperature on the charging/discharging processes in PECVD silicon nitride films based on induced surface potential and adhesive force measurements using atomic force microscopy**

Heiba Zaghoul, George Papaioannou, Bharat Bhushan, Haixia Wang, Fabio Coccetti, Patrick Pons, Robert Plana

► **To cite this version:**

Heiba Zaghoul, George Papaioannou, Bharat Bhushan, Haixia Wang, Fabio Coccetti, et al.. Effect of deposition reactive gas ratio, RF power and substrate temperature on the charging/discharging processes in PECVD silicon nitride films based on induced surface potential and adhesive force measurements using atomic force microscopy. *Journal of Microelectromechanical Systems*, 2011, 20 (6), pp.1395-1417. hal-00670055

**HAL Id: hal-00670055**

**<https://hal.science/hal-00670055>**

Submitted on 14 Feb 2012

**HAL** is a multi-disciplinary open access archive for the deposit and dissemination of scientific research documents, whether they are published or not. The documents may come from teaching and research institutions in France or abroad, or from public or private research centers.

L'archive ouverte pluridisciplinaire **HAL**, est destinée au dépôt et à la diffusion de documents scientifiques de niveau recherche, publiés ou non, émanant des établissements d'enseignement et de recherche français ou étrangers, des laboratoires publics ou privés.

**Effect of deposition reactive gas ratio, RF power and substrate temperature on the charging/discharging processes in PECVD silicon nitride films based on induced surface potential and adhesive force measurements using Atomic force microscopy**

U. Zaghoul<sup>1,2,3</sup>, G.J. Papaioannou<sup>1,2,4</sup>, B. Bhushan<sup>3\*</sup>, H. Wang<sup>1,2</sup>, F. Coccetti<sup>1,2,5</sup>, P. Pons<sup>1,2\*</sup>, and R. Plana<sup>1,2</sup>

<sup>1</sup>CNRS ; LAAS ; 7 avenue du colonel Roche, F-31077 Toulouse, France

<sup>2</sup>Université de Toulouse ; UPS, INSA, INP, ISAE ; LAAS ; F-31077 Toulouse, France

<sup>3</sup>NLBB Laboratory, The Ohio State University, Columbus, OH 43210, USA

<sup>4</sup>University of Athens, Solid State Physics, Panepistimiopolis Zografos, Athens, Greece

<sup>5</sup>Novamems, 10 av. De l'Europe, F-31520 Toulouse, France

**Abstract:**

The dependence of the electrical properties of silicon nitride on the deposition conditions used to prepare it and consequently on material stoichiometry has not been fully understood. In the present study, the influence of plasma-enhanced chemical vapor deposition (PECVD) conditions on the dielectric charging of SiN<sub>x</sub> films is investigated. The work targets mainly the dielectric charging phenomenon which constitutes a major failure mechanism in electrostatically driven MEMS devices, particularly in electrostatic capacitive MEMS switches. The charging/discharging processes in the investigated SiN<sub>x</sub> films have been studied using two different nanoscale characterization techniques based on Kelvin probe force microscopy (KPFM) and, for the first time, force-distance curve (FDC) measurements. The main advantage of the FDC based methodology is that it takes into account the meniscus force between the AFM tip and the SiN<sub>x</sub> surface which cannot be measured by KPFM. The electrical properties of the SiN<sub>x</sub> films obtained from both techniques show a very good correlation. X-ray photoelectron spectroscopy (XPS) and Fourier transform infra-red spectroscopy (FT-IR) material characterization techniques have been also used to determine the compositions and chemical bonds, respectively, of the SiN<sub>x</sub> films. An attempt to correlate between the chemical and electrical properties of SiN<sub>x</sub> films is made.

**Keywords:** Silicon nitride; dielectric charging; force-distance curve; adhesive force; Kelvin probe microscopy; electrostatic MEMS; RF MEMS switch; Reliability

\* Corresponding authors: [Bhushan.2@osu.edu](mailto:Bhushan.2@osu.edu), [ppons@laas.fr](mailto:ppons@laas.fr)

## 1. Introduction

Among other reliability issues, the dielectric-charging phenomenon is well identified as a major reliability concern for numerous electrostatically driven MEMS devices, particularly for electrostatic MEMS switches (Rebeiz, 2003). Charge build up with time in the dielectric film leads to high adhesion or stiction between the suspended electrode and the dielectric surface and results in the failure of the switch (Wibbeler et al., 1998; Rottenberg et al., 2004; Spengen et al., 2004; Goldsmith et al., 2007, Zaghoul et al., 2010a, 2011b). On the way to solving this problem, several dielectric materials have been investigated, among which the most intensively investigated ones are  $\text{SiO}_2$  and  $\text{Si}_3\text{N}_4$ . In contrast to the extensive knowledge gathered on their electrical properties, and stemming from semiconductor technology, a comprehensive understanding of the charging phenomenon is still missing. This is why these materials still cannot provide a successful solution for the dielectric charging problem. This is attributed to the fact that in MEMS the dielectric films are deposited on rough substrates, typically with low temperature processes, which leads to significant deviation from material stoichiometry. Besides, the presence of hydrogen, introduced during the film deposition, significantly affects the dielectric charging due to its non-negligible diffusion (Shea et al., 2004).

Charging phenomenon in dielectric films used in MEMS arises from dipoles orientation and charge injection, displacement and trapping that occurs under the strong electric field during the down-state position (Papaioannou et al., 2005). The charge transport/redistribution was reported to follow the Poole-Frenkel effect, as found from the dependence of the shift of pull-out voltage on the actuation bias (Melle et al., 2005). In  $\text{SiN}_x$  material it is reported that “holes injection” introduces metastable traps (Lau et al., 1998; Shannon et al., 1994). These metastable defects affect the charge transport in the dielectric (Nieuwesteeg et al., 1992) and give rise to asymmetrical current-voltage characteristics in metal-insulator-metal (MIM) capacitors, a commonly used device for studying the bulk properties of dielectric layers with electrode material symmetry (Venderschueren et al., 1979). It has been shown also that the relaxation time of charged  $\text{SiN}_x$  layers increases with the applied electric field intensity (Zaghoul et al., 2009a, 2011b).

Significant research has been performed to identify the dependence of dielectric charging on material stoichiometry and its relation to the deposition parameters in the case of PECVD  $\text{SiN}_x$  films (Lamhamdi et al., 2008; Zaghoul et al., 2009a, 2011b,d; Daigler et al., 2009;

Tavassolian et al. 2009; Koutsourelis et al., 2011). The stored charge was found to increase almost linearly with increasing film thickness for low frequency (LF) SiN<sub>x</sub> material, while there was no clear effect of the dielectric film thickness on the stored charge in the case of high frequency (HF) material (Daigler et al., 2009; Zaghoul et al., 2009a). The injected charge density was reported to be smaller and the relaxation process was found to be faster in HF SiN<sub>x</sub> material compared to LF SiN<sub>x</sub> (Zaghoul et al., 2010c, 2011b,d). Moreover, the stored charge was found to increase with increasing SiN<sub>x</sub> deposition temperature (Daigler et al., 2009; Tavassolian et al., 2009), a behavior which was attributed to increasing the nitrogen content in the SiN<sub>x</sub> material with the temperature (Tavassolian et al., 2009). The high deposition temperature has been reported to reduce the hydrogen concentration and particularly decrease N–H bonds compared to Si–H bonds films (Herth et al., 2010). Also, the charging of SiN<sub>x</sub> has been reported to increase when the silicon content increases in spite of the increasing leakage current (Koutsourelis et al., 2011). The impact of surface and bulk leakage currents on the chemical modification of the dielectric film surface and charge accumulation have been discussed by Shea et al. (2004). In spite of all of these efforts, the dependence of the dielectric charging in SiN<sub>x</sub> films on material stoichiometry and its relation to the deposition parameters which affect the concentration of bulk and interface traps as well as the concentration of dipoles and charge accumulation is not fully understood.

A variety of characterization methodologies have been employed in order to assess the dielectric charging phenomenon (Zaghoul et al., 2010b). For example, current measurements in MIM capacitors have been introduced by Yuan et al. (2005), Lamhamdi et al. (2006, 2008), Papandreou et al. (2007), Daigler et al. (2009), and Zaghoul et al. (2009a), while capacitance and/or voltage measurements in MEMS capacitive switches are reported by Melle et al. (2005), Papaioannou et al. (2005), Herfst et al. (2006), and Ruan et al. (2008). The mentioned methods, although extremely useful, lead to results that depend strongly on the nature of the device under test. Thus, in MIM capacitors the discharge takes place under a short circuit condition, and the injected charges are collected by the injecting electrodes. On the contrary, in MEMS the injected charges are collected only by the bottom electrode while the top electrode, the bridge, is in the up-state. Additionally, MEMS failure mechanisms are often related to multiphysics phenomena. As a matter of fact fatigue and creep and other thermally induced failure modes mix up with the dielectric charging failure mode and yield a shift on the bias parameters of the device.

Therefore, the characterization techniques which make use of MEMS switches cannot study accurately the dielectric charging phenomenon since other failure mechanisms contribute to the measurements. Besides, they are quite expensive and time consuming techniques since they require the fabrication of the complete MEMS devices, including many levels of photolithography.

More recently, Kelvin probe force microscopy (KPFM) has been employed and shown to be a promising method in the dielectric charging assessment for several reasons. First, it efficiently simulates charging and discharging conditions of MEMS capacitive switches, providing qualitative information on dielectric free surface charge distribution and decay (Lamhamdi et al., 2007; Belarni et al., 2008; Zaghoul et al., 2008, 2009b, 2010a, 2011b). KPFM has been used also to study the discharging process on a microscopic scale in charged dielectric films implemented in MEMS switches (Herfst et al., 2008, Zaghoul et al., 2011d). The second reason is that KPFM based methodology provides a low cost and quite fast solution compared to the currently available assessment methods since the required samples for this approach consist only of thin dielectric films deposited over planar substrates, and no photolithography steps are required during the sample preparation (Zaghoul et al., 2010c). In addition, the use of such techniques allow studying separately the dielectric charging physics, and hence building a comprehensive understanding of the charging phenomenon without interference with other failure mode physics. Yet, the influence of meniscus force between the AFM tip and the sample surface cannot be measured using KPFM. Zaghoul et al. (2011c) has recently reported that in a MEMS switch, the meniscus formation resulting from the adsorbed water film between the switch bridge and the dielectric layer and its related electric field-induced meniscus constitutes major force components which contribute heavily to the final measured adhesive force. Based on that, a characterization technique which is capable of measuring the influence of meniscus force and at the same time could investigate the dielectric charging phenomenon becomes essential.

In view of the presented problems, the aim of the present work is to provide a deeper insight into the influence of the deposition parameters of PECVD SiN<sub>x</sub> films on both material stoichiometry as well as charging/discharging processes. Different deposition recipes have been employed, including variable reactive gas ratio, RF power, and substrate temperature. The charging/discharging processes have been studied using two different characterization techniques

based on KPFM and, for the first time, FDC measurements. The main advantage of the FDC technique is that it takes into account the meniscus force between the AFM tip and the  $\text{SiN}_x$  surface which cannot be measured by KPFM. X-ray photoelectron spectroscopy (XPS) and Fourier transform infra-red spectroscopy (FT-IR) material characterization techniques have been used to determine the compositions and chemical bonds, respectively, of the  $\text{SiN}_x$  films. The presented study could help to determine which dielectric is more robust for electrostatic MEMS with better reliability.

The article is organized as follows. First, the investigated samples as well as the different employed characterization techniques are presented in the experimental section. This is followed by a detailed section for the results and discussion. Finally, a conclusion of the study is presented.

## **2. Experimental approach**

In this section, the PECVD deposition parameters as well as the layer structure of the investigated samples is presented first. This is followed by introducing the two employed electrical characterization techniques based on KPFM and FDC measurements. Finally, the FT-IR and XPS measurement parameters are presented.

### *2.1 Samples*

The investigated samples consist of PECVD  $\text{SiN}_x$  films with 200 nm thickness deposited over 500 nm Au layers, which were evaporated over Si substrates as shown in **Fig. 1a**. The  $\text{SiN}_x$  layers were deposited using a PECVD reactor (STS, Multiplex Pro-CVD). This reactor has a pair of 8" size upper and bottom electrodes made of stainless steel used within the deposition chamber, which is kept at high vacuum during the deposition process. The main feature of this deposition system is its duality of RF operation modes, namely low frequency (LF) at 380 kHz and high frequency (HF) at 13.56 MHz. Also, the operating power can be adjusted to range from 0 to 1000 W in the LF mode and from 0 to 600 W in the HF mode. Other features of the system include the pressure ranging from 0 to 2000 mTorr,  $\text{SiH}_4$  flow rates ranging from 0 to 500 sccm,  $\text{NH}_3$  flow rates ranging from 0 to 360 sccm, and  $\text{N}_2$  flow rates varying from 0 to 5000 sccm.

During the deposition process silane ( $\text{SiH}_4$ ) and ammonia ( $\text{NH}_3$ ) are used as the reactive species, while nitrogen ( $\text{N}_2$ ) is used as a dilution gas.  $\text{SiN}_x$  films were deposited using different

deposition parameters by changing individually the gas ratio (SiH<sub>4</sub>/NH<sub>3</sub>), RF power, and substrate temperature. The explored process parameters are the following: (1) gas ratio (SiH<sub>4</sub>/NH<sub>3</sub>) varying from 0.15 to 0.8, (2) RF power varying from 20 W to 100 W, and (3) substrate temperature varying from 200 °C to 300 °C. **Table 1** lists the deposition parameters which were used in this study. The last sample in **Table 1** represents a reference sample and is common for the three varied deposition parameters. The detailed PECVD deposition conditions for this reference sample are listed in **Table 2**. All other SiN<sub>x</sub> samples have been deposited using the same N<sub>2</sub> flow, chamber pressure, and radio frequency mode (HF) listed in **Table 2**.

## 2.2 KPFM-based characterization

In this methodology, charges are first injected in single points over the SiN<sub>x</sub> surface by applying voltage pulses of defined amplitude, U<sub>p</sub>, and duration, T<sub>p</sub>, to the AFM tip during scanning the sample surface in tapping mode (**Fig. 1a**). After completing the charge injection, KPFM surface potential measurement is performed using the lift-mode (Zaghloul et al. 2010a, 2011b). In such a mode the topography and the potential signals are subsequently recorded. SCM-PIT metal coated conductive tips from Veeco have been used for these measurements. The time interval between the end of the charge injection step and the beginning of the KPFM measurement is fixed to be 30 s for all experiments.

In KPFM measurements, three spectral components for the electrostatic force between the AFM tip and the sample surface exist at DC, ω and 2ω, where ω is the mechanical resonance frequency of the AFM cantilever. Since the cantilever responds only to forces at or very close to its resonance frequency, the DC and F<sub>2ω</sub> force components do not cause any significant oscillation of the cantilever, and F<sub>ω</sub> becomes the dominant one and is given by Jacobs et al. (1997), DeVecchio and Bhushan (1998), Bhushan and Goldade (2000), and Bhushan (2011)

$$F_{\omega} = -\frac{dC}{dz}(\Delta\Phi - U_{DC})U_{AC} \cos(\omega t) \quad (1)$$

where C is the capacitance between the tip and the sample surface, z is the tip-sample separation, ΔΦ is the contact potential difference between the tip and the sample material, U<sub>DC</sub> is the applied DC voltage to the AFM tip from the KPFM feedback loop, and U<sub>AC</sub> is the amplitude of the sinusoidal signal applied from the oscillator to drive the AFM tip at or very close to its mechanical resonance frequency, ω, during the surface potential measurements. The main goal

of the KPFM feedback loop is to adjust the potential of the tip,  $U_{DC}$ , until the term  $\Delta\Phi - U_{DC}$  becomes 0, at which point the cantilever oscillation amplitude should be zero ( $F_0 = 0$ ). At this point, the measured tip potential,  $U_{DC}$ , which corresponds to the contact potential difference between the tip and the sample,  $\Delta\Phi$ , is equal to the sample surface potential, and is used to generate a potential map for the sample surface. Due to trapped charges in the  $\text{SiN}_x$  film which results from the charge injection step, the contact potential difference between the tip and the dielectric film,  $\Delta\Phi$ , is altered, and is determined by the local measured tip potential,  $U_{DC}$ .

For each injected point, the measured surface potential,  $U_{DC}$ , has a maximum at the position which was directly under the AFM tip apex during the charge injection step, and it decreases gradually at the edges of injected position (Jacobs et al. 1998; Zaghloul et al., 2010a, 2011b). The peak value of the induced surface potential is located in the KPFM map, and a horizontal cross section is taken at this position resulting in an absolute surface potential profile. In order to eliminate the impact of the tip material, the background surface potential of the  $\text{SiN}_x$  film has been measured first before performing the charge injection step. Then, the background potential has been subtracted from the absolute potential profile resulting in the relative surface potential which is a direct indication of the injected charge density in the dielectric film. Therefore, the analysis of results is performed through the surface potential peak amplitude,  $U_s$ , the full width at half maximum (FWHM), and the integral of the measured relative potential profile (**Fig. 1b**). For better accuracy, each KPFM measurement has been performed three times, and a statistical evaluation for  $U_s$ , FWHM, and the potential profile integral has been made by averaging over these three measurements. The evolution of  $U_s$ , FWHM, and the potential profile integral with time have been also monitored and analyzed. Though the data analysis could be done based on the potential profile integral only, the extracted  $U_s$  and FWHM are also presented in order to show the charge distribution over the dielectric films.

A sample of the measured KPFM surface potential maps for charges which have been injected using different pulse amplitude,  $U_p$ , and using positive and negative voltage is presented in **Fig. 2a,b**. The figure also shows the potential maps obtained at different time points after the charge injection step. The decay of the measured surface potential with time due to charge collection is obvious from the figure. **Fig. 2c** presents the resulting potential profile for the  $\text{SiN}_x$  samples deposited using different reactive gas ratio for charges which have been injected under the same pulse amplitude (40 V). It is clear from the figure that  $U_s$ , FWHM, and consequently

the integral of the potential profile, which is a direct indication for the injected charge density inside the dielectric film, changes remarkably with the deposition gas ratio.

### 2.3 FDC based characterization

The adhesive force between the AFM tip and the  $\text{SiN}_x$  film has been calculated from force-distance curve (FDC) measurements (Bhushan, 2010, 2011). An example of the force-distance curve for the investigated samples is presented in **Fig. 3a**. The force-distance measurement starts at a large separation from the sample surface (point A) where there is no deflection of the cantilever. As the piezo moves towards the sample, a sudden mechanical instability occurs between point B and point C, and the tip jumps into contact with the adsorbed water film and wicks up around it to form a meniscus. The cantilever bends downwards because of the attractive meniscus force acting on the tip. As the piezo further approaches the  $\text{SiN}_x$  surface, the deflection of the cantilever increases while the tip travels in the water film and eventually contacts the underlying  $\text{SiN}_x$  surface at point C, and then the cantilever starts to bend upwards. Once the piezo reaches the end of its designated ramp size at point D, it is retracted to its starting position. The tip goes beyond zero deflection (point E) and enters the adhesion region. At point E, the elastic force of the cantilever becomes equivalent to the adhesive force, causing the cantilever to snap back to point F. The adhesive force, which is the force needed to pull the tip away from the sample, can be calculated from the force-distance curve by multiplying the vertical distance between E and F with the stiffness of the cantilever as explained in **Fig. 3a** (Bhushan, 2010, 2011).

When voltage is applied between the AFM tip and the AFM base chuck, which is connected to the Au layer underneath the  $\text{SiN}_x$  film, the cantilever deflection increases due to the increase in the attractive electrostatic force as shown in **Fig. 3b**. The difference between points E and F increases too with increasing the applied voltage as shown from the figure and this leads to an increase in the adhesive force between the AFM tip and the dielectric film. Basically, this is the principle behind which the FDC technique was employed to study the dielectric charging phenomenon. In this methodology the charging of the  $\text{SiN}_x$  film is performed through scanning a selected area over its surface ( $10\ \mu\text{m} \times 10\ \mu\text{m}$ ) using an AFM tip in contact mode while a voltage difference is applied between the tip and the Au layer underneath the  $\text{SiN}_x$  film. Then the force-volume method was used to obtain the adhesive force map over the charged dielectric area

(Bhushan, 2011; Zaghloul et al., 2011c). Before charging the SiN<sub>x</sub> surface, the adhesive force map was first measured which represents the adhesion due to meniscus formation. This force component is then subtracted from the resulting adhesive force after the charge injection step. Therefore, the adhesive force data presented in this paper represents mainly the attractive electrostatic force between the AFM tip and the sample surface which results from charging the dielectric film.

A sample of the obtained adhesive force maps is shown in **Fig. 3b** showing that the adhesive force in the charged areas is much larger compared to non-charged areas over the dielectric surface. Charge injection over the dielectric surface results in a large induced surface potential over the dielectric film which causes a considerable voltage difference between the AFM tip and the sample. Consequently the electrostatic attractive force between the AFM tip and the dielectric surface will increase, causing the net adhesive force to be larger than non-charged areas. For each adhesive map a statistical evaluation has been performed by averaging over all the measured positions in each map. After completing the charge injection step of the SiN<sub>x</sub> film, the discharging process has been studied through measuring adhesive force maps continuously for the charged area with time. This has been performed using a modified force-volume technique in order to reduce the influence of the grounded AFM tip on the discharging process. The FDC experiments have been performed using highly doped Si tips, FORTA-10 (resistivity 0.01-0.025 ohm/cm, tip radius < 10 nm, spring constant 1.2-6.4 N/m).

The induced surface potential over the dielectric surface resulting from the charging step was measured using a novel methodology which is based also on the force-distance curve measurements. As shown from **Fig. 3b** when voltage difference exists between the AFM tip and the sample, the cantilever does not return directly to its original position and instead its return path has an intermediate stag. Also, the induced surface potential has an opposite polarity of the voltage used for the charging step. Based on that, after completing the dielectric charging the external applied voltage used during the charging step is reduced gradually in order to set off the induced surface potential over the dielectric surface. When the applied bias equals the induced surface potential, force distance curve returns to its original shape and the intermediate stages shown in **Fig. 3b** disappear. At that point, the external applied voltage is equal in amplitude and opposite in sign to the induced surface potential over the dielectric surface. The potential levels which could be measured using this technique is much larger compared to what could be

measured using the KPFM. With the used tips which have an average spring constant of 3 N/m the best obtained accuracy of this technique was around 1.2V, much larger compared to KPFM. Yet, it is believed that the accuracy could be enhanced by using tips with much smaller stiffness. The other main advantage of this technique is its capability to measure accurately the surface potential at higher relative humidity levels compared to KPFM which could not work properly at larger humidity levels due to the potential shielding effect (Sugimura et al., 2002).

The relative humidity is found to have a very high influence on the charging/discharging processes in SiN<sub>x</sub> thin films (Zaghloul et al., 2009c, 2011a). Also, the removal of the water-related layer from both surfaces on the sample and the AFM tip is reported to be very important to improve the reliability of the KPFM measurements (Ono et al., 2001). Moreover, it has been reported that larger humidity levels and thicker adsorbed water film over the sample surface results in larger adhesive force between the AFM tip and the sample surface (Zaghloul et al., 2011c). This adhesive force increases remarkably when voltage is applied between the tip and the sample due to the formation of electric field induced meniscus (Zaghloul et al., 2011c). For these reasons, both the SiN<sub>x</sub> samples and the AFM tip went through two cycles of heating (150 °C) and cooling steps under vacuum in order to avoid the influence of humidity and the adsorbed water film over the dielectric surface on both KPFM and FDC measurements. In addition, both KPFM and FDC experiments have been performed under dry air flow (relative humidity ≈ 0.02%) using a controlled environment AFM chamber as presented in (Zaghloul et al., 2011a). A commercial AFM (NanoScope® IIIa MultiMode™ with Extender™ Electronics Module) has been used to perform the KPFM and FDC measurements in this study. The tips used in these experiments have been calibrated continuously before each measurement through measuring the KPFM surface potential and the adhesive force for a standard sample for the KPFM and FDC experiments, respectively.

#### *2.4 Physical material characterization*

Two material characterization techniques have been used; FT-IR and XPS. FT-IR spectroscopy has been performed to provide information about the chemical bonds of the dielectric film and their variations. The infrared spectra were acquired in reflection mode in the 400 – 4000 cm<sup>-1</sup> range with BIORAD FTS60A spectrometer with the samples under nitrogen flow to avoid the effect of humidity and ambient. The XPS experiments have been used to

provide information about the different chemical bonds and valence state in the SiN<sub>x</sub> surface and then in depth through sputtering. A VG ESCALAB 220-iXL spectrometer has been used to perform the XPS measurements. The deposited SiN<sub>x</sub> layers were excited by MgK $\alpha$  (1253.6 eV), and the kinetic energies of the electrons emitted were collected at a constant energy resolution of 1 eV. The energy step used to record the spectra was 0.2 eV. Since the SiN<sub>x</sub> films are rather nonconductive, electron compensation was used during the measurement. The atomic concentration of the investigated SiN<sub>x</sub> films measured by XPS is presented in **Table 1**. The N/Si ratio obtained for all deposited layers shows a strong silicon excess compared to the stoichiometric composition (1.33). Since the hydrogen content in the film will affect the silicon excess, a particular attention has been drawn on the Si–H and N–H bonds obtained from FT-IR.

### 3. Results and discussion

The influence of the AFM tip on the charge collection process as well as a comparison between the data obtained from KPFM and FDC assessment methodologies is presented first. This is followed by discussing the influence of the reactive gas ratio, RF power, and substrate temperature on the dielectric charging.

#### 3.1 KPFM versus adhesive force measurements

**Figure 4** presents a sample of the surface potential decay with time for charges which have been injected using different pulse amplitudes,  $U_p$ . For this kind of experiment, the dielectric surface was scanned with time just after the charge injection step in order to monitor the discharging process. As shown from the figure, the surface potential amplitude,  $U_s$ , decreases (**Fig. 4a**) while the potential distribution, FWHM, increases (**Fig. 4b**) with time. The integral of the corresponding potential profile for these data, which is a direct indication of the charge density in the dielectric film, is presented in **Fig. 4c**. The figure highlights that the measured charge density decreases with time, indicating that the injected charge is being collected or removed with time.

In order to quantify the influence of the AFM tip on the charge collection process a separate experiment similar to the one presented by Ziegler et al. (2008) has been performed. Charges have been injected over the SiN<sub>x</sub> using the same charge injection parameters used in the previous experiment. Instead of scanning the dielectric surface continually with time as normally

done for other decay experiments, the surface potential was measured only directly after the charge injection step and then at the end of the observation time window (3.5 hours). During this period the AFM tip was disengaged far from the sample surface in order to avoid affecting the charge collection process. The resulting  $U_s$ , FWHM, and integral of potential profiles for this experiment directly after the charge injection step and at the end of the experiment is plotted in **Fig. 4 a, b, and c**, respectively, with solid symbols. The figure highlights clearly that the measured  $U_s$ , FWHM, and the potential profile integral for the natural decay is slightly larger than their corresponding values for KPFM decay (where the sample surface was scanned continually with time). This indicates that the grounded tip, which is employed in conventional tapping mode for topography imaging during the first pass of the KPFM lift mode, contributes to the charge collection process due to charge transfer between dielectric and tip. The normalized values of the potential profile integral obtained from both experiments (natural decay and KPFM decay) are plotted in **Fig. 4d**. The figure highlights obviously that the injected charge density in the cases of natural decay is slightly larger compared to KPFM decay, and this is observed for charges which have been injected under different pulse amplitude. For example, for charges injected at  $U_p = 40$  V, the potential profile integral for the natural decay and KPFM decay is reduced to 0.82 and 0.80, respectively. This small difference could be neglected, and it confirms that studying the discharging process in electrostatic MEMS switches by monitoring the evolution of KPFM surface potential with time is a very efficient methodology. KPFM simulates to a great extent the charge collection scenario which takes places in MEMS switches where the injected charge is collected by the bottom electrode when the switch bridge is in the Up state.

The discharge process in  $\text{SiN}_x$  films has been also investigated by monitoring the evolution of the adhesive force between the AFM tip and the dielectric surface with time. The observation time window here was 1 hour in order to get enough data points which are required for the fitting as will be explained later. **Fig. 5a** presents an example of adhesive force decay with time measured using the FDC technique for charges injected using 40 V. As charges are collected with time, the surface potential over the dielectric surface decreases, and this results in reducing the potential difference between the AFM tip and the dielectric surface with time too. Therefore, the electrostatic attractive force between the AFM tip and the sample surface will decrease with time, and this causes the decrease in the adhesive force with time as shown from the figure. Here it should be highlighted that the parameters of adhesive force measurements

with time have been optimized in order to reduce the influence of the grounded AFM tip on the charge collection process. Moreover, the observation time window used for these experiments (1 hour) is shorter than the time window used for the KPFM decay experiments (3.5 hours). **Fig. 5b** shows the normalized adhesive force decay for charges which have been injected using different voltage for the same  $\text{SiN}_x$  sample used in **Fig. 4**. For the sake of comparison with KPFM decay, the corresponding values of the integral of KPFM potential profiles after a time period of 1 hour from the charging step are plotted in the figure. Though the comparison between decay data from both techniques (KPFM and FDC) is difficult considering that the measured physical quantity is different in both techniques, **Fig. 5b** shows a good correlation between the normalized data obtained from both techniques. For example, it is obvious from the figure that the charge collection process as measured by both techniques becomes longer as the voltage amplitude used during the charging step increases.

### *3.2 Effect of reactive gas ratio*

For these samples, the deposition RF power and substrate temperature were kept constant while the gas ratio was varied as shown in **Table. 1**. In this section the results obtained from KPFM and FDC measurements are presented first. This is followed by presenting the influence of the gas ratio on the material stoichiometry based on FT-IR and XPS data. The correlation between the electrical and chemical characterization results is then discussed.

#### *3.2.1 KPFM results*

**Figure 6** presents the influence of the reactive gas ratio  $\text{SiH}_4/\text{NH}_3$  on the charging (left) and discharging (right) processes, as extracted from the KPFM measurements for charges which have been injected using different pulse amplitude. It could be observed from **Fig. 6a** that the measured surface potential amplitude,  $U_s$ , decreases gradually when the gas ratio increases from 0.15 to 0.45, and this is followed by a sudden decrease to a very close value from 0 for 0.6 and 0.8 gas ratios. Also, the charge distribution represented by the FWHM decreases gradually as the gas ratio increases from 0.15 to 0.8 as highlighted in **Fig. 6b**. The integral of the resulting potential profile (**Fig. 6c**) shows clearly that the injected charge density decreases gradually as the gas ratio increases from 0.15 to 0.45 and then shows a very high reduction when the gas ratio

increases beyond 0.45. These remarks have been observed for injected charges under different pulse amplitude.

A sample of the surface potential evolution with time for SiN<sub>x</sub> films deposited using different gas ratio is shown in **Fig. 6d**. The figure presents the normalized value of the surface potential with respect to the maximum U<sub>s</sub> measured directly after completing the charge injection step (at t=0), and it highlights clearly that the surface potential decay becomes faster as the gas ratio increases. The sudden decrease in the relaxation time when increasing the gas ratio from 0.45 to 0.6 and 0.8 is also obvious from the figure. The surface potential decays exponentially

with time following the stretched exponential law,  $\exp\left[-\left(\frac{t}{\tau}\right)^\beta\right]$ , where  $\tau$  is the process time

constant, and  $\beta$  ( $0 \leq \beta \leq 1$ ) is the stretch factor (Phillips, 1996; Zaghloul et al., 2010a,c, 2011b). This is observed for all investigated SiN<sub>x</sub> samples in this study and for charges which have been injected under different pulse amplitudes, U<sub>p</sub>. The decay time constant and stretch factor calculated from the surface potential decay data for SiN<sub>x</sub> samples deposited with different gas ratios is shown in **Figs. 6e,f**, respectively. The y-axis of the **Fig. 6e** is plotted in log scale, and it highlights clearly the huge variation in the relaxation time constant when changing the gas ratio. The decay time constant decreases gradually when increasing the gas ratio from 0.15 to 0.45 and then features a sudden decrease when the gas ratio reaches 0.6 and 0.8, which agrees with the data presented in **Fig. 6d**. No clear effect of the gas ratio on the stretch factor is found as shown in **Fig. 6f**. The trend of the decay time constant and stretch factor versus the gas ratio is found to be similar for charges which have been injected using different pulse amplitude, U<sub>p</sub>. Due to the fast charge collection process at higher gas ratios (0.6 and 0.8), the obtained data points for the surface potential evolution with time for several pulse amplitudes for these samples were not sufficient to fit with the stretched exponential equation. Finally, the decay time constant increases while the stretch factor decreases when larger pulse amplitudes are used during the charging step, which is attributed to the lowering of potential barrier for charge emission from band gap states due to the Poole–Frenkel effect (Simmons, 1967) as presented in details in previous work (Zaghloul et al., 2009a, 2011b, 2011d).

### 3.2.2 FDC results

The impact of the gas ratio on the charging/discharging processes based on force distance curve (FDC) measurements is presented in **Fig. 7**. The correlation between the measured FDC potential and the FDC adhesive force as a function of the reactive gas ratio and/or the voltage applied during the charge injection is quite obvious. As the induced surface potential increases, the adhesive force between the AFM tip and the SiN<sub>x</sub> surface increases too as observed from the figure. The adhesive force between the AFM tip and the dielectric film has three main components. The first component is the liquid mediated meniscus force caused by meniscus formation between the AFM tip and the dielectric surface. The second force component resembles the attractive electrostatic force between the AFM tip and the SiN<sub>x</sub> surface due to the dielectric charging. The third force component is the field induced meniscus which results from the influence of the electric field on the meniscus formation (Calleja et al., 2002; Gómez-Moñivas et al., 2003; Sacha et al., 2006). The contribution of the liquid mediated meniscus and the field induced meniscus to the measured adhesive force is minimal in this study due to the dehydration step done for the investigated samples as well as performing the adhesive force experiments under very low relative humidity levels as reported by Zaghoul et al. (2011c). Based on that, the increase in the measured adhesive force with the induced potential is attributed mainly to the increase in the attractive electrostatic force. Comparing **Figs. 7a,b** with **Fig. 6c**, it is obvious that the trend of the measured CPD potential and adhesive force versus the reactive gas ratio agrees quite well with the trend of the integral of the potential profile KPFM.

An example of the evolution of the measured adhesive force with time for SiN<sub>x</sub> samples deposited using different a gas ratio is presented in **Fig. 7c**. It is found that the decay of the adhesive force with time fits very well with the square of the stretched exponential equation

$(\exp\left[-\left(\frac{t}{\tau}\right)^\beta\right])^2$ . Since the KPFM surface potential fits properly with the normal stretched

exponential equation  $\exp\left[-\left(\frac{t}{\tau}\right)^\beta\right]$ , this confirms undoubtedly that the measured adhesive force

between the AFM tip and the SiN<sub>x</sub> surface resembles mainly the attractive electrostatic force.

The calculated decay time constant from the adhesive force evolution with time is shown in **Fig. 7d**. It is obvious from the figure that the trend of the decay time constant versus the reactive gas ratio agrees well with the trend obtained from KPFM surface potential decay (**Fig. 6e**). This has

been observed for charges injected using different voltage levels. The other interesting point here is that the decay time constant and the stretch factor extracted from fitting the adhesive force evolution with time are found to increase and decrease, respectively, as found from the KPFM surface potential decay. Here it should be highlighted that the shorter decay time constant calculated from the adhesive force decay compared to the time constant calculated from KPFM surface potential decay does not indicate a faster charge collection than KPFM potential decay. As presented in **Fig. 5**, the decay of the adhesive force and KPFM potential is almost comparable. The considerable difference in the decay time constant calculated from FDC and KPFM is attributed mainly to the different equations used for the fitting process in each case. Obviously, the square of the stretched exponential equation leads to much smaller decay time constant for the same decay data.

In conclusion, both employed characterization techniques based on KPFM and FDC measurements leads to the same conclusion regarding the electrical properties of the  $\text{SiN}_x$  films deposited using different reactive gas ratio. The injected charge density as well as the relaxation time decrease gradually when the gas ratio increases from 0.15 to 0.45, and then decrease sharply for the 0.6 and 0.8 gas ratios. Since the FDC measurements efficiently simulate the operation of MEMS switches, the nanoscale characterization on the level of a single asperity is proved to be an excellent approach to understand the charging/discharging phenomenon which takes place on the device level.

### 3.2.3 Influence on material stoichiometry

The FT-IR spectra for  $\text{SiN}_x$  films deposited using different gas ratio are presented in **Fig. 8a**. The layer compositions with different gas flow ratios, in particular the change of Si–H (around  $2157\text{ cm}^{-1}$  at  $70^\circ$ ,  $2160\text{ cm}^{-1}$  at  $20^\circ$ ) and N–H (around  $3348\text{ cm}^{-1}$  at  $70^\circ$ ,  $3350\text{ cm}^{-1}$  at  $20^\circ$ ) from FT-IR with N and Si atomic fractions determined by XPS analysis are shown in **Figure 8b**. In the as-deposited layers the N/Si content (about 0.845 for  $r = 0.15$ , and 0.63 for  $r = 0.80$ ) decreases linearly with the gas ratio. The relative intensity of Si–H versus N–H vibrations increases quite sharply, which shows N–H molecules are reduced. It is consistent with the corresponding lower amount of nitrogen in the higher gas ratio. Thus, silicon content increases with the amount of  $\text{SiH}_4$  gas.

On the other hand, the observation of a strong increase of the Si–H relative signal amplitude in the larger gas ratio suggests that Si atoms with more dangling bonds are present in large amounts in the matrix. As a consequence of reduced N/Si ratio, seen in **Fig. 8a**, the absorption peak of Si–N vibrations tend to lie in the lower frequency from  $r = 0.15$  at LO mode  $1029 \text{ cm}^{-1}$ , to  $r = 0.8$  at  $1016 \text{ cm}^{-1}$ . Meanwhile, the rocking mode =N-H (at  $1214 \text{ cm}^{-1}$ ,  $1201 \text{ cm}^{-1}$ ,  $1183 \text{ cm}^{-1}$ ,  $1177 \text{ cm}^{-1}$  for  $r = 0.15, 0.25, 0.6, 0.8$ , respectively) increases in the relative amplitude and shift to high frequency indicating that the involvement of more nitrogen in the silicon nitride thin films as the gas ratio decreases. The trend described above is in agreement with the high frequency shift of SiN-H<sub>2</sub> bending mode at  $1553 \text{ cm}^{-1}$  to  $1528 \text{ cm}^{-1}$  with reduced gas ratio. The interesting point is Si-H may have a slight shift to high frequency with more nitrogen backbond, but for the N-H bonds which will always be in the same configuration Si<sub>2</sub>N-H, no such effect will be observed. The two large peaks of LO and TO mode of Si-N stretching vibration were observed, which are definitely related to SiN<sub>x</sub> phonon spectra. Although in the present amorphous silicon nitride the long range order no longer exists, the short-range may be similar to the crystalline part. At high gas ratio, the nitrogen atoms are scarce and the vibration mode of isolated Si-N<sub>x</sub> network is local, which is similar to the zone boundary mode of crystalline silicon nitride. When more nitrogen atoms are incorporated into the film as the gas ratio decreases, the Si-N<sub>x</sub> network become extended and similar to the zone center mode of Si<sub>3</sub>N<sub>4</sub>, and the high frequency shoulder appears.

### 3.2.4 Discussion

Charges in the dielectric reduce the interface (electrode/insulator) electric field, and this reduces the injection rate/efficiency. This is mainly because the injected charges are most probably located very close to the injecting electrodes (Papaioannou et al., 2010). The charge injection rate is compensated by charge redistribution rate. Charge redistribution takes place through various mechanisms, i.e. Poole-Frenkel, hopping, leakage, etc. The injected charge saturation is determined by the rate of charge injection and redistribution. The magnitude of injected charge density is obtained by the continuity equation of these two mechanisms during charging, if no equilibrium is reached:  $\nabla J = \frac{d\rho}{dt} \neq 0$ , where  $J = J_{charge} - J_{discharge}$ , and  $\rho$  is the

density of charge per unit volume. At saturation at any point  $\nabla J = \frac{d\rho}{dt} = 0$ , the total current (from charge injection plus redistribution) at that point. This equilibrium is determined by the charging electric field and charging time. It is also affected by charge trapping centers characteristics and trapped charge distribution which are dependent on the material stoichiometry.

The silicon content in the investigated SiN<sub>x</sub> films increases with the SiH<sub>4</sub>/NH<sub>3</sub> gas ratio as seen from **Fig. 8b**. Increasing the silicon content or equivalently decreasing the nitrogen content in SiN<sub>x</sub> films has been reported to increase the leakage current as measured from current-voltage characteristics in MIM capacitors (Koutsourelis et al., 2011). This basically is attributed to the formation of nanoclusters (Carrada et al., 2008; Petersen et al., 2006; Vishnyakov et al., 2009; Gritsenko et al., 2004) and traps which allow the charge transport through conductive percolation tunneling paths and hopping through defect states (Cen et al., 2009). Increasing the silicon content also results in increasing the concentration of defects (Koutsourelis et al., 2011) and leads to a larger number of charge trapping centers (Ackaerta et al., 2008). This results in increasing the density of traps, as well as the probability of percolation and hopping. Charge redistribution paths, therefore, increase and the redistribution becomes easier as the silicon content in the dielectric film increases. Consequently the redistribution current will be larger and will lead to a smaller charge density at the dielectric surface. For this reason, the charge injection/redistribution equilibrium will be attained at a smaller surface charge density. For smaller gas ratio (for example  $r = 0.15$ ) the silicon content is reduced and the material goes near from stoichiometry with less leakage and defect concentration. Thus, the charge redistribution paths will decrease, resulting in a smaller redistribution current and consequently larger charge density at the dielectric surface. The equilibrium between charge injection/redistribution is therefore obtained at a larger surface charge density.

The measured surface potential by KPFM and/or FDC measurements and consequently the adhesive force between the AFM tip and the dielectric film represents mainly the charge density at, or very close to the dielectric surface. In view of the above analysis, for small gas ratio ( $r = 0.15$ ) with less silicon content, the charge redistribution is small, and this results in slow charge collection process by the bottom electrode. This explains the longer decay time constant in the case of smaller gas ratio compared to larger gas ratio simply because the

discharge rate depends on the discharge time constant. It also explains why the injected charge density, surface potential, and consequently the adhesive force between the AFM tip and the SiN<sub>x</sub> surface are larger for smaller gas ratios compared to larger ones. Here it should be highlighted that the results presented in this study based on KPFM and FDC measurements regarding the influence of the gas ratio are in good agreement with data presented in Koutsourelis et al. (2011). In the mentioned study the bias at which the measured TSDC current is zero in MIM capacitor implementing PECVD SiN<sub>x</sub> films is found to decrease with decreasing the nitrogen content in the SiN<sub>x</sub> film, a behavior which is attributed to an increase in the leakage current. The presented result is in good agreement with Ackaerta et al. (2008) where increasing the gas ratio (SiH<sub>4</sub>/NH<sub>3</sub>) results in increasing the leakage current density. The results agree as well with the work presented by Zaghoul et al. (2011b) where SiN<sub>x</sub> films with more silicon content exhibits a smaller injected charge density and a faster charge decay.

### *3.3 Effect of RF power*

For these samples, the deposition RF power and substrate temperature were kept constant while the gas ratio was varied as shown in **Table 1**.

#### *3.3.1 KPFM results*

The influence of the deposition RF power on the charging and discharging processes as measured by KPFM surface potential is presented in **Fig. 9 left and right**, respectively. The measured surface potential, U<sub>s</sub>, does not exhibit a clear trend as the RF power increases for injected charges under different pulse amplitude, U<sub>p</sub>. A similar remark is observed for the trend of the potential distribution, FWHM, versus RF power. Additionally, the trend of surface potential amplitude, U<sub>s</sub>, and distribution, FWHM, is not consistent for some data points. For example the U<sub>s</sub> decreases while the FWHM increases when the RF varies from 60 W to 80 W. An opposite trend for both U<sub>s</sub> and FWHM is observed, however, when increasing the RF power from 80 W to 100 W. Here it should be highlighted that the variation of both U<sub>s</sub> and FWHM with RF power for injected charges under different pulse amplitude is smaller compared to their variation as a function of the gas ratio (**Fig. 6a,b**). This is more evident for the potential distribution variation as a function of the gas ratio (**Fig. 6b**) and RF power (**Fig. 9b**).

The integral of the KPFM potential profile for different RF power is shown in **Fig. 9c**. The figure highlights that the injected charge density slightly increases when the RF power increases from 20 W to 40 W. Further increase in the RF power leads to a slight decrease in the injected charge density until the 80 W RF power is reached. The injected charge density is shown to increase once again when the RF power increases from 80 W to 100 W. Here it should be pointed out that the variation of the injected charge density with RF power is relatively small compared to its change versus the reactive gas ratio (**Fig. 6c**), and this is observed for charges injected under different pulse amplitude. Moreover, the almost horizontal fitting lines shown in **Fig. 9c** points out that the investigated range of deposition RF power in this study has a minimal influence on the injected charge density. Finally, negative charge injection has relatively larger injected charge density compared to positive charge injection for the whole investigated RF power values, except for the 60 W point where positive and negative charge injection exhibit a comparable values. This is observed for injected charges using different pulse amplitude.

An example of the KPFM surface potential decay for  $\text{SiN}_x$  films deposited using different RF power is presented in **Fig. 9d**. The figure highlights that the charge collection process becomes relatively faster when increasing the deposition RF power. This is evident from the decay time constant calculated for this set of samples for charges injected under different pulse amplitude as shown in **Fig. 9e**. Comparing **Fig. 9e** and **Fig. 6e**, it is concluded that the influence of the gas ratio on reducing the decay time constant is much larger compared to the impact of the RF power. The stretch factor,  $\beta$ , shows also a decreasing trend as the deposition RF power increases as shown in **Fig. 9f**. In previous studies (Papaioannou et al., 2005; Zaghloul et al., 2009a, 2011b,d) the stretch factor,  $\beta$ , has been used as an index of charge collection complexity. The decrease of the stretch factor points out that the discharge process deviates from the simple exponential law (where  $\beta = 1$ ), and hence the charge collection mechanism becomes more complex. **Figs. 9e,f** shows also that for each deposition RF power, the decay time constant increases while the stretch factor decreases when the pulse amplitude employed during the charge injection step increases as reported by Zaghloul et al. (2010c, 2011b,d).

### 3.3.2 FDC results

**Figure 10** presents the influence of the deposition RF power on the charging/discharging processes in  $\text{SiN}_x$  films as obtained from FDC measurements. No clear trend for the measured

FDC potential with RF power for charges which have been injected using different voltage as shown in **Fig. 10a**. This is in agreement with the trend of the KPFM potential profile integral presented in **Fig. 9c**. Also, the variation of the measured FDC potential with the deposition RF power is relatively small compared to its change as a function of the reactive gas ratio (**Fig. 7a**). The measured adhesive force as a function of the deposition RF power is shown in **Fig. 10b**, and it also exhibits a very good correlation with the measured CPD potential for injected charges under different voltage. Comparing **Fig. 7b** and **Fig. 10b**, it is obvious that the influence of the deposition RF power on the adhesive force between the AFM tip and the dielectric surface is relatively smaller compared to the effect of the gas ratio.

An example of the adhesive force decay for  $\text{SiN}_x$  films deposited under different RF power is presented in **Fig. 10c**. It could be seen from the figure that the rate of charge collection process slightly increases when the deposition RF power increases. This is evident from the decay time constant calculated from the adhesive force evolution for  $\text{SiN}_x$  samples deposited using different RF power for charges injected under different voltage as shown in **Fig. 10d**. Comparing **Fig. 10d** and **Fig. 7d**, it could be concluded that the influence of the reactive gas ratio on the discharging process is much larger than the impact of the deposition RF power. Also, the correlation between the decay time constant versus the deposition RF power calculated from the FDC adhesive force evolution with time (**Fig. 10d**) and the time constant extracted from the KPFM surface potential decay (**Fig. 9e**) is obvious. The difference in values between the decay time constant extracted from both techniques is related mainly to the different equation used for data fitting as explained earlier.

### 3.3.3 Influence on material stoichiometry

**Figure 11a** presents the FT-IR spectra for  $\text{SiN}_x$  films deposited using different RF power. The layers with  $r = 0.45$  constant value which are obtained at different operation power in **Fig. 11b** give rise to a slight move up of N/Si atomic ratio. It shows a weak increase of the N content and slight decrease of silicon with the power increase for the lower power 20 with a N/Si value about 0.694, and then it reaches 0.728 at the power 100 W. On the other hand, there is an opposite trend in the relative intensity of Si-H (around  $2160 \text{ cm}^{-1}$ ) versus N-H (around  $3330 \text{ cm}^{-1}$ ) with plateau character. These behaviors correspond to the relatively reduced Si contents in the two power ends. Indeed, the stoichiometric compositions of the layers are very close, as

confirmed by the FT-IR measurements. The remarkable change occurs in the layers with the highest power 100, which LO mode shows a slight shift to high frequency (at  $1036\text{ cm}^{-1}$  for power 40 to  $1048\text{ cm}^{-1}$  for power 100) and also relatively increased intensity considering LO mode SiN at  $1048\text{ cm}^{-1}$  versus the =N-H rocking vibration at about  $1185\text{ cm}^{-1}$ .

#### 3.3.4 Discussion

The difference in the injected charge density and charge collection process obtained by KPFM and FDC results for  $\text{SiN}_x$  samples deposited using different RF power, though small, cannot be fully explained in view of the data obtained by FT-IR and XPS, which leads to the conclusion that the stoichiometric compositions of these films are very close. However, it should be mentioned that the hydrogen content in the investigated films in this study was not quantified since the XPS measurement is not sensitive to hydrogen or helium. Also there is no report on the dependence of the dielectric charging in  $\text{SiN}_x$  films deposited using different RF power on the hydrogen content. On the other side, the density and distribution of defects in  $\text{SiN}_x$  films is expected to be larger as the deposition RF power increases. This could affect the charge injection as well as the charge collection process. Additionally, the higher the employed RF power is, the higher the deposition rate which normally results in larger disorder due to higher energy transfer to Si and N atoms during the deposition process (Zaghloul et al., 2011b). The larger density of defects indicates that the charge redistribution paths are larger leading to higher redistribution currents. Consequently, this results in faster charge decay as the deposition RF power increases as obtained from the evolution of KPFM surface potential and FDC adhesive force with time.

The injected charge density was expected to increase as the RF power increases due to the higher density of defects which exists in  $\text{SiN}_x$  films deposited at larger RF power. This is observed only when the RF power changes from 20 W to 40 W and then from 80 W to 100 W as shown from the KPFM results (**Fig. 9c**) and FDC measurements (**Fig. 10a,b**). Changing the RF power from 40 W to 80 W passing through 60 W shows a continuous decrease in the injected charge density. The decreasing trend of the injected charge density when increasing the RF power from 40 W to 80 W could be explained based on the equilibrium between charge injection and redistribution as explained in detail in **section 3.2.4**. Since the charge collection process becomes faster as the RF power increases indicating larger redistribution paths and consequently larger redistribution currents, the charge injection and redistribution equilibrium is attained at

smaller surface charge density. This results in decreasing the measured KPFM potential and/or FDC adhesive force when increasing the RF power in this range. The variation in the injected charge density when changing the RF power from 20 W to 40 or from 80 W to 100 W does not follow this rule most probably due to a larger defect density which could lead to higher stored charge.

### *3.4 Effect of temperature*

For these samples, the deposition gas ratio and RF power were kept constant while the substrate temperature was varied as shown in **Table 1**.

#### *3.4.1 KPFM results*

The KPFM results related to the charging/discharging processes in SiN<sub>x</sub> films deposited using different substrate temperature is presented in **Fig. 12**. The surface potential amplitude, U<sub>s</sub>, distribution, FWHM, and the integral of potential profile slightly decrease with increasing the substrate temperature from 200 °C to 300 °C as shown in **Figs. 12a, b and c**, respectively. This indicates that the injected charge density slightly decreases as the substrate temperature gets higher in this investigated temperature range, and this is observed for charge injected under different pulse amplitude. Comparing these results with the KPFM data extracted from SiN<sub>x</sub> samples deposited using different gas ratio (**Fig. 6a, b and c**) leads to the conclusion that the influence of the substrate temperature on the charging process is much less compared to the effect of the reactive gas ratio. The difference in injected charge density between positive and negative charge injection is quite obvious for SiN<sub>x</sub> films deposited at 200 °C, while this difference decreases considerably as the deposition temperature increases to 250 °C or 300 °C.

An example of the KPFM surface potential evolution with time for SiN<sub>x</sub> films deposited using different substrate temperatures is shown in **Fig. 12d**. It can be seen from the figure that the charge collection process becomes faster as the deposition temperature increases from 200 °C to 300 °C. This is evident from the decay time constant values calculated from the surface potential decay for charges injected using different pulse amplitude as shown in **Fig. 12e**. No clear trend is found for the stretch factor calculated for this set of samples as a function of the substrate temperature as presented in **Fig. 12f**. **Figure 12e,f** shows also that for each deposition temperature the decay time constant increases while the stretch factor decreases when the pulse

amplitude employed during the charge injection step increases as reported by Zaghoul et al. (2011b,d). Comparing the decay time constant calculated from KPFM surface potential decay for SiN<sub>x</sub> samples deposited using different gas ratio (**Fig. 6e**), RF power (**Fig. 9e**), and substrate temperature (**Fig. 12e**), it could be concluded that the influence of the substrate temperature on the charge collection process is relatively larger than the effect of the RF power and much smaller compared to the influence of the gas ratio.

### 3.4.2 FDC results

The influence of the substrate temperature employed during the SiN<sub>x</sub> deposition on the charging/discharging process as extracted from the FDC measurements is presented in **Fig. 13**. The measured FDC potential (**Fig. 13a**) and adhesive force (**Fig. 13b**) slightly decreases when the substrate temperature increases from 200 °C to 300 °C for charges injected using different voltage. The correlation between the FDC measured potential and adhesive force is also obvious from the figures. Moreover, the trend of both FDC potential and adhesive force versus the substrate temperature agree well with the trend of KPFM potential profile integral (**Fig. 12c**) indicating a relatively smaller injected charge density as the deposition temperature increases in the investigated range. Comparing the values of the FDC potential and adhesive force measured for SiN<sub>x</sub> samples deposited using different gas ratio (**Fig. 7a,b**) and substrate temperature (**Fig. 13 a,b**) leads to the conclusion that the influence of the substrate temperature on the charging process is relatively small compared to the effect of the gas ratio, which is also concluded from the KPFM measurements.

A sample of the measured adhesive force decay for SiN<sub>x</sub> films deposited using different substrate temperature is presented in **Fig. 13c**. The relaxation process becomes faster as the deposition temperature increases from 200 °C to 300 °C as shown in the figure. The decay time constant calculated from the adhesive force evolution with time for charges injected using different pulse amplitude is presented in **Fig. 13c**. The figure also highlights a faster charge collection process as the substrate temperature increases, which agrees well with the results obtained from KPFM measurements. Comparing the decay time constant calculated from adhesive force evolution with time for SiN<sub>x</sub> samples deposited using different gas ratio (**Fig. 7c**), RF power (**Fig. 10c**), and substrate temperature (**Fig. 13c**) leads to the conclusion that the effect of the substrate temperature on the charge collection process is relatively larger than the effect of

the RF power and much smaller compared to the influence of the gas ratio. This is also similar to the conclusion drawn from the KPFM surface potential measurements.

### 3.4.3 Influence on material stoichiometry

The FT-IR spectra for SiN<sub>x</sub> films deposited using different substrate temperature is shown in **Fig. 14a**. The increased deposition temperature from 200 °C, then 250 °C to 300 °C at the same gas ratio  $r = 0.45$  led to no pronounced fall-down of N/Si atomic ratio (0.694 to 0.681) as shown from **Table 1** and **Fig. 14b**. From FT-IR spectra, LO mode of Si-N at 1027 cm<sup>-1</sup> at 250 °C increases to 1051 cm<sup>-1</sup> at 300°C, and oppositely the = N-H rocking vibration becomes weak, (1188 cm<sup>-1</sup> at 250°C, 1181 cm<sup>-1</sup> at 300°C). In this case, the highest deposition temperature demonstrated a similar effect as in the film with the maximum deposition power 100 W. The increased deposition temperature tends to reduce the reaction of NH<sub>3</sub> gas, and also reduce the content of hydrogen in all plasma deposited materials, which leads to more preferred formation of nitrogen and silicon N<sub>x</sub>-Si-H bonds ( $x \geq 2$ ). Since the nitrogen is more electronegative than silicon, the incorporation of nitrogen leads to an increase in the frequency of the absorption peak. Although the shift of N-H stretching vibrations is not conspicuous, it is believed that this is due to the emergence of the NH<sub>2</sub> asymmetric mode. As supporting evidence, the NH<sub>2</sub> bending mode at about 1539 cm<sup>-1</sup> disappeared at the highest temperature 300 °C.

### 3.4.4 Discussion

From KPFM and FDC measurements it is concluded that increasing the substrate temperature results in slightly reducing the injected charge density and making the charge collection process relatively faster. This indicates that the charge redistribution is relatively larger with higher deposition temperature resulting in attaining equilibrium between the charge injection and redistribution at smaller surface potential amplitude as explained earlier. From the data presented in Tavassolian et al. (2009), the measured TSDC current at 300 K for the SiN<sub>x</sub> deposited at 200 °C is found to be slightly larger compared to at 300 °C. This agrees with the results obtained from the measurements which were performed at room temperature. As seen from FT-IR and XPS data, increasing the deposition temperature from 200 °C, then 250 °C to 300 °C at the same gas ratio  $r = 0.45$  lead to non-pronounced variation in the N/Si atomic ratio. This shows a good agreement with the data presented in Tavassolian et al. (2009) where the N/Si

is shown not to vary much and also does not have a consistent trend in the range of 200 °C to 300 °C deposition temperature.

The difference between the charging/discharging processes for SiN<sub>x</sub> films deposited using different temperatures could be attributed to several reasons. First, the increased deposition temperature is known to cause desorption of hydrogen in PECVD silicon nitride, which results in reducing the hydrogen content in the film. For example, the hydrogen content decreases from 26.88% for SiN<sub>x</sub> films deposited at 200 °C to 11.66% for the films deposited at 340 °C (Herth et al., 2010). For this reason the possible contribution from hydrogen migration to the dielectric charging in SiN<sub>x</sub> films deposited using different substrate temperatures cannot be overruled. Second, the influence of the film stress on the material electrical properties, and hence on the dielectric charging, has to be considered. Increasing the deposition temperature results in changing the film stress from compressive stress for films deposited at 100 °C to tensile when the deposition was performed at 300 °C (Papandreou et al., 2007). It has been also reported that the residual stress of SiN<sub>x</sub> films increases from 110 MPa to 530 MPa as the SiN<sub>x</sub> film growth temperature increases from 200 °C to 340 °C (Herth et al., 2010). The deposition temperature and pressure was also reported to have a considerable effect on the material structure and mechanical properties (Thornton, 1977; Bhushan and Gupta, 1991). The third reason could be attributed to the difference in trap concentrations between the SiN<sub>x</sub> samples deposited at different temperatures (Tavassolian et al., 2009). Here, it should be emphasized that presently there is no report on the dependence of silicon nitride charge trap concentration and properties on the material stoichiometry and bandgap. Finally, increasing the deposition temperature results in reducing the SiN<sub>x</sub> film conductivity (Herth et al., 2010) because hydrogen is known for its chemical reactivity creating Si–H bonds rather than N–H bonds (Lamhamdi et al., 2006). This is expected also to affect the dielectric charging. Many of these hypotheses require further investigation in order to fully understand the influence of the deposition temperature on the dielectric charging.

The amount of Si–H and N–H bonds in all investigated SiN<sub>x</sub> samples in this study indicates that there is a high concentration of Si matrix that is not bound to N, which can in principle give rise to Si cluster nucleation. It is in agreement with the results discussed above which show all silicon-rich type with N/Si ratio much less than stoichiometric one (1.33). Changing the gas ratio has a much stronger effect on the material composition and structural

properties compared to the effect of RF power and substrate temperature. Comparing the  $\text{SiN}_x$  layers deposited with variable RF power and substrate temperature at the same gas ratio  $r = 0.45$ , it is found that their compositions remain almost in the same domain around 0.7. Further investigation is currently in progress for the  $\text{SiN}_x$  films deposited with the extreme deposition parameters (RF power 100 W, substrate temperature 300 °C) which have a microscopic structural change.

#### 4. Conclusion

The influence of PECVD deposition conditions on the dielectric charging of  $\text{SiN}_x$  films has been investigated. Numerous  $\text{SiN}_x$  films have been deposited using different recipes including variable silane/ammonia gas ratio, RF power, and substrate temperature. The study targets mainly the dielectric charging phenomenon in electrostatically actuated MEMS devices, particularly electrostatic capacitive MEMS switches. The charging/discharging processes in the investigated  $\text{SiN}_x$  films have been studied using two different characterization techniques based on Kelvin probe force microscopy (KPFM) and, for the first time, force-distance curve (FDC) measurements. The main advantage of the FDC-based assessment methodology is that it takes into account the meniscus force between the AFM tip and the  $\text{SiN}_x$  surface which exists in MEMS switches between the switch bridge and the dielectric surface and cannot be measured by KPFM. Fourier transform infra-red spectroscopy (FT-IR) and X-ray photoelectron spectroscopy (XPS) material characterization techniques have been used to determine the chemical bonds and compositions, respectively, of the  $\text{SiN}_x$  films being investigated. An attempt to correlate between the chemical and electrical properties of  $\text{SiN}_x$  films is performed.

The charge relaxation process has been studied through monitoring the time evolution of KPFM surface potential and, for the first time, by measuring the evolution of adhesive force with time. The evolution of KPFM surface potential follow properly with the stretched exponential equation, while the decay of the adhesive force with time is found to fit well with the square of the stretched exponential equation. This indicates that the measured adhesive force between the AFM tip and the  $\text{SiN}_x$  surface in this study resembles mainly the attractive electrostatic force. The characterization of the charging/discharging processes in dielectric films based on adhesive force measurements is presented in this study for the first time.

The injected charge density as well as the relaxation time constant decreases gradually when the  $\text{SiH}_4/\text{NH}_3$  gas ratio increases from 0.15 to 0.45, and then decreases sharply for the 0.6 and 0.8 gas ratios. This is attributed to increasing the silicon content in the investigated  $\text{SiN}_x$  films with increasing the gas ratio as seen from FT-IR and XPS data, which results in larger leakage current, higher concentration of defects and larger number of charge trapping centers. Charge redistribution paths, therefore, increase, and consequently the redistribution current will be larger and will lead to a smaller charge density at the dielectric surface. For this reason, the charge injection/redistribution equilibrium, which determines the magnitude of injected charge density measured by KPFM or FDC, will be attained at a smaller surface charge density with larger gas ratio.

The difference in the injected charge density and charge collection process obtained from KPFM and FDC measurements for  $\text{SiN}_x$  samples deposited using different RF power, though small, cannot be fully explained in view of the data obtained by FT-IR and XPS, which leads to the conclusion that the stoichiometric compositions of these films are very close. However, it should be mentioned that the hydrogen content in the investigated films in this study was not quantified. The density and distribution of defects in  $\text{SiN}_x$  films is expected to be larger as the deposition RF power increases. This results in larger charge redistribution paths, higher redistribution currents, and consequently faster charge decay as the deposition RF power increases. The results from the KPFM and FDC measurements lead to the conclusion that increasing the substrate temperature from 200 °C to 300 °C results in slightly reducing the injected charge density and making the charge collection process relatively faster, in spite of the non-pronounced variation in N/Si atomic ratio for these samples as obtained by FT-IR and XPS. This indicates that the charge redistribution is relatively larger with higher deposition temperature which results in attaining the charge injection/redistribution equilibrium at smaller charge density at the dielectric surface. This is attributed mainly to reducing the hydrogen content in the  $\text{SiN}_x$  film, increasing the film stress, changing trap concentrations, and reducing film conductivity when deposition temperature increases.

KPFM and FDC data shows clearly that the influence of the reactive gas ratio on the charging/discharging process in  $\text{SiN}_x$  films is much larger compared to the effect of substrate temperature and RF power. This is in good agreement with the results obtained from FT-IR and XPS which highlights that the reactive gas ratio has a larger influence on the  $\text{SiN}_x$  material

stoichiometry compared to the effect of RF power or substrate temperature. On the other side, both employed characterization techniques based on KPFM and FDC measurements leads to similar conclusions regarding the charging/discharging processes in the investigated  $\text{SiN}_x$  films deposited using different gas ratio, RF power, and temperature. Since the FDC-based characterization efficiently simulates the operation of MEMS switches, the KPFM nanoscale characterization performed on the level of a single asperity is proved to be an excellent approach to understand the dielectric charging phenomena which takes place on the device level.

The study provides a deeper insight to the dielectric charging phenomenon based on novel characterization methodologies. Considering the lack of available information on the dependence of silicon nitride charge trap concentration and electrical properties on the material stoichiometry and its relation to the dielectric deposition conditions, this work could help to determine which dielectric is more robust for electrostatic MEMS devices with better reliability.

### **Acknowledgments**

This work has been partially supported by the following projects: the French ANR project FAME (PNANO-059), POLYNOE project funded by European Defense Agency (B-0035-IAP1-ERG), and the SYMIAE project funded by the Fondation STAE.

## References

- Ackaerta, J., R. Charavela, K. Dhondta, B. Vlachakisa, L. De Scheppera, M. Millecama, et al. (2008) "MIMC reliability and electrical behavior defined by a physical layer property of the dielectric," *J. Microelectron. Reliab.* **48**, 1553-1556.
- Belarni, A., M. Lamhamdi, P. Pons, L. Boudou, J. Guastavino, Y. Segui, G. Papaioannou and R. Plana (2008), "Kelvin probe microscopy for reliability investigation of RF-MEMS capacitive switches," *J. Microelectron. Reliab.* **48**, 1232-1236.
- Bhushan, B. (2010), *Springer Handbook of Nanotechnology*, third edition, Springer-Verlag, Heidelberg, Germany.
- Bhushan, B. (2011), *Nanotribology and Nanomechanics I - Measurement Techniques and Nanomechanics, II – Nanotribology, Biomimetics, and Industrial Applications*, Third ed., Springer-Verlag, Heidelberg, Germany.
- Bhushan, B., and B. K. Gupta (1991), *Handbook of Tribology: Materials, Coatings, and Surface Treatments*, McGraw-Hill, New York.
- Bhushan, B. and A. Goldade (2000), "Measurements and analysis of surface potential change during wear of single-crystal silicon (100) at ultralow loads using Kelvin probe microscopy," *App. Surf. Sci.* **157**, 373-381.
- Calleja, M., M. Tello, and R. García (2002), "Size determination of field-induced water menisci in noncontact atomic force microscopy," *J. Appl. Phys.* **92**, 5539-5542.
- Carrada, M., A. Zerga, M. Amann, J. J. Grob, J. P. Stoquert, A. Slaoui, C. Bonafos, and S. Scham (2008), "Structural and optical properties of high density Si-ncs synthesized in SiN<sub>x</sub>:H by remote PECVD and annealing," *Mater. Sci. Eng., B* **147**, 218-221.
- Cen, Z. H., T. P. Chen, L. Ding, Y. Liu, J. I. Wong, M. Yang, Z. Liu, W. P. Goh, Z. H. F. R. Zhu, and S. Fung (2009), "Evolution of electroluminescence from multiple Si-implanted silicon nitride films with thermal annealing," *J. Appl. Phys.* **105**, Art. # 123101.
- Daigler, R., E. Papandreou, M. Koutsourelis, G. Papaioannou and J. Papapolymerou (2009), "Effect of deposition conditions on charging processes in SiN<sub>x</sub>: Application to RF-MEMS capacitive switches," *J. Microelectron. Eng.* **86**, 404-407.
- DeVecchio, D. and B. Bhushan (1998), "Use of a nanoscale Kelvin probe for detecting wear precursors," *Rev. Sci. Instrum.* **69**, 3618-3624.
- Gritsenko, V. A., D. V. Gritsenko, Yu. N. Novikov, R. W. M. Kwok, and I. Bello, (2004), "Short-range order, large-scale potential fluctuations, and photoluminescence in amorphous SiN<sub>x</sub>," *J. Exp. Theor. Phys.* **98**, 760-769.
- Goldsmith, C., D. Forehand, Z. Peng, J. Hwang and I. Ebel (2007), "High-cycle life testing of RF MEMS switches," *2007 IEEE MTT-S Int. Microwave Symp. Proc.*, pp. 1805-1808, IEEE, New York.
- Gómez-Monivas, S., J. J. Sáenz, M. Calleja, and R. Garcia (2003), "Field-Induced Formation of Nanometer-Sized Water Bridges," *Phys. Rev. Lett.* **91**, 056101.
- Herfst, R., H. Huizing, P. Steeneken and J. Schmitz (2006), "Characterization of dielectric charging in RF MEMS capacitive switches," *Proc. of the IEEE Int. Conf. on Microelectronic Test Structures*, pp. 133-136, IEEE, New York.
- Herfst, R., P. Steeneken, J. Schmitz, A. Mank and M. van Gils (2008), "Kelvin probe study of laterally inhomogeneous dielectric charging and charge diffusion in RF MEMS capacitive switches," *2008 IEEE Int. Reliability Physics Symposium Proc. 46th Annual (IRPS 2008)*, pp. 492-495, IEEE, New York.

- Herth, E., B. Legrand, L. Buchailot, N. Rolland, and T. Lasri (2010), "Optimization of SiN<sub>x</sub>: H films deposited by PECVD for reliability of electronic, microsystems and optical applications," *J. Microelectron. Reliab.* **50**, 1103-1106.
- Jacobs, H. O., H. F. Knapp, S. Müller and A. Stemmer (1997), "Surface potential mapping: A qualitative material contrast in SPM," *Ultramicroscopy* **69**, 39-49.
- Jacobs, H. O., P. Leuchtman, O. J. Homan and A. Stemmer (1998), "Resolution and contrast in Kelvin probe force microscopy," *J. Appl. Phys.* **84**, 1168–73.
- Koutsourelis, M., N. Tavassolian, G. Papaioannou, and J. Papapolymerou (2011), "Dielectric charging in capacitive microelectromechanical system switches with silicon nitride," *Appl. Phys. Lett.* **98**, Art. # 093505.
- Lamhamdi, M., J. Guastavino, L. Boudou, Y. Segui, P. Pons, L. Bouscayrol and R. Plana (2006), "Charging-Effects in RF capacitive switches influence of insulating layers composition," *J. Microelectron. Reliab.* **46**, 1700-1704.
- Lamhamdi, M., L. Boudou, P. Pons, J. Guastavino, A. Belarni, M. Dilhan, Y. Segui and R. Plana (2007), "Si<sub>3</sub>N<sub>4</sub> thin films properties for RF-MEMS reliability investigation," *Proc. of the International Solid-State Sensors, Actuators and Microsystems Conference, 2007 (TRANSDUCERS 2007)*, pp. 579-582, IEEE, New York.
- Lamhamdi, M., P. Pons, U. Zaghoul, L. Boudou, F. Coccetti, J. Guastavino, Y. Segui, G. Papaioannou and R. Plana (2008), "Voltage and temperature effect on dielectric charging for RF-MEMS capacitive switches reliability investigation," *J. Microelectron. Reliab.* **48**, 1248-1252.
- Lau, S., J.M. Shannon and B.J. Sealy (1998), "Changes in the Poole–Frenkel coefficient with current induced defect band conductivity of hydrogenated amorphous silicon nitride," *J Non-Cryst Solids* **277-230**, 533–537.
- Melle, S., D. De Conto, D. Dubuc, K. Grenier, O. Vendier, J. Muraro, J. Cazaux and R. Plana (2005), "Reliability modeling of capacitive RF MEMS," *IEEE Trans. on Microw. Theory Tech.* **53**, 3482-3488.
- Nieuwesteeg, K., J. Boogaard, G. Oversluizen and M. Powell (1992), "Current stress induced asymmetry in hydrogenated amorphous silicon n i n devices," *J. Appl. Phys.* **71**, 1290-1297.
- Ono, S., M. Takeuchi and T. Takahashi (2001), "Kelvin probe force microscopy on InAs thin films grown on GaAs giant step structures formed on (110) GaAs vicinal substrates," *Appl. Phys. Lett.* **78**, 1086-1088.
- Papaioannou, G., M. Exarchos, V. Theonas, G. Wang and J. Papapolymerou (2005), "Temperature study of the dielectric polarization effects of capacitive RF MEMS switches," *IEEE Trans. Microw. Theory Tech.* **53**, 3467-3473.
- Papaioannou, G., F. Coccetti and R. Plana (2010), "On the Modeling of Dielectric Charging in RF-MEMS Capacitive Switches," *10th topical meeting on silicon monolithic integrated circuits in RF Systems (SIRF)*, New Orleans, pp.108-111.
- Papandreou, E., M. Lamhamdi, C. M. Skoulikidou, P. Pons, G. Papaioannou and R. Plana (2007), "Structure dependent charging process in RF MEMS capacitive switches," *J. Microelectron. Reliab.* **47**, 1812-1817.
- Petersen, M., and Y. Roizin, (2006), "Density functional theory study of deep traps in silicon nitride memories ," *Appl. Phys. Lett.* **89**, Art. # 053511.
- Phillips, J. (1996), "Stretched exponential relaxation in molecular and electronic glasses," *Rep. Prog. Phys.* **59**, 1133-1207.

- Rebeiz, G. M. (2003), *RF MEMS theory, design, and technology*, John Wiley & Sons, Inc., Hoboken, New Jersey.
- Rottenberg, X., B. Nauwelaers, W. De Raedt and H. Tilmans (2004), "Distributed dielectric charging and its impact on RF MEMS devices," *Proc. of the 34th European Microw. conf.*, pp. 77-80, IEEE, New York.
- Ruan, J., G. J. Papaioannou, N. Nolhier, N. Mauraun, M. Bafleur, F. Coccetti and R. Plana (2008), "ESD failure signature in capacitive RF MEMS switches," *J. Microelectron. Reliab.* **48**, 1237-1240.
- Sacha, G. M., A. Verdaguer, and M. Salmeron (2006), "Induced Water Condensation and Bridge Formation by Electric Fields in Atomic Force Microscopy," *J. Phys. Chem. B*, **110**, 14870-14873.
- Shannon, J., S. C. Deane, B. McGarvey, and J. N. Sandoe (1994), "Current induced drift mechanism in amorphous SiNx:H thin film diodes," *Appl. Phys. Lett.* **65**, 2978.
- Shea, H. R., A. Gasparyan, H. B. Chan, S. Arney, R. E. Frahm, D. López, S. Jin, and R. P. McConnell (2004), "Effects of electrical leakage currents on MEMS reliability and performance," *IEEE Trans. Device Mater. Reliab.* **4**, 198 - 207.
- Simmons, J. G. (1967), "Poole-Frenkel Effect and Schottky Effect in Metal-Insulator-Metal Systems," *Phys. Rev.* **155**, 657-660.
- Spengen, W., R. Puers, R. Mertens and I. Wolf (2004), "A comprehensive model to predict the charging and reliability of capacitive RF MEMS switches," *J. Micromech. Microeng.* **14**, 514-521.
- Sugimura, H., Y. Ishida, K. Hayashi, O. Takai and N. Nakagiri (2002), "Potential shielding by the surface water layer in Kelvin probe force microscopy," *Appl. Phys. Lett.* **80**, 1459-1461.
- Tavassolian, N., M. Koutsourelis, E. Papandreou, G. Papaioannou, B. Lacroix, Z. Liu, and J. Papapolymerou (2009), "The effect of silicon nitride stoichiometry on charging mechanisms in RF-MEMS capacitive switches," *IEEE Trans. Microwave Theory Tech.* **57**, 3518 - 3524.
- Thornton, J. A. (1977), "High rate thick film growth," *Ann. Rev. Mater. Sci.*, **7**, 239-260.
- Venderschueren, J. and J. Casiot In (1979): P. Braunlich, Editor, *Thermally stimulated relaxation in solids*, Springer-Verlag, Heidelberg, Germany.
- Vishnyakov, A. V., Yu. N. Novikov, V. A. Gritsenko, and K. A. Nasyrov (2009), "The charge transport mechanism in silicon nitride: Multi-phonon trap ionization," *Solid-State Electron.* **53**, 251-255.
- Wibbeler, J., G. Pfeifer and M. Hietschold (1998), "Parasitic charging of dielectric surfaces in capacitive microelectromechanical systems (MEMS)," *Sens. Actuator A-Phys.* **71**, 74-80.
- Yuan, X., J. Hwang, D. Forehand and C. Goldsmith (2005), "Modeling and characterization of dielectric-charging effects in RF MEMS capacitive switches," *2005 IEEE MTT-S Int. Microwave Symp. Dig.*, pp. 753-756, IEEE, New York.
- Zaghloul, U., A. Abelarni, F. Coccetti, G. Papaioannou, R. Plana and P. Pons (2008), "Charging processes in silicon nitride films for RF-MEMS capacitive switches: The effect of deposition method and film thickness," *Microelectromechanical Systems-Materials and Devices II, MRS Proc. Vol. 1139*, (eds. S. M. Spearing, S. Vengallatore, N. Sheppard and J. Bagdahn), pp. 141-146, Material Research Society (MRS), Pennsylvania.

- Zaghloul, U., G. Papaioannou, F. Coccetti, P. Pons and R. Plana (2009a), "Dielectric charging in silicon nitride films for MEMS capacitive switches: Effect of film thickness and deposition conditions," *J. Microelectron. Reliab.* **49**, 1309-1314.
- Zaghloul, U., A. Belarni, F. Coccetti, G. Papaioannou, L. Bouscayrol, P. Pons and R. Plana (2009b), "A comprehensive study for dielectric charging process in silicon nitride films for RF MEMS switches using Kelvin probe microscopy," *2009 Int. Solid-State Sensors, Actuators and Microsystems Conf. (TRANSDUCERS 2009)*, pp. 789-793, IEEE, New York.
- Zaghloul, U., G. Papaioannou, F. Coccetti, P. Pons and R. Plana (2009c), "Effect of Humidity on Dielectric Charging Process in Electrostatic Capacitive RF MEMS Switches Based on Kelvin Probe Force Microscopy Surface Potential Measurements," *Microelectromechanical Systems-Materials and Devices III, MRS Proc. Vol. 1222*, (eds. J. Bagdahn, N. Sheppard, K. Turner and S. Vengallatore), pp. 39-44, Material Research Society(MRS), Pennsylvania.
- Zaghloul, U., G. J. Papaioannou, F. Coccetti, P. Pons and R. Plana (2010a), "A systematic reliability investigation of the dielectric charging process in electrostatically actuated MEMS based on Kelvin probe force microscopy " *J. Micromech. Microeng.* **20**, Art.# 064016.
- Zaghloul, U., M. Koutsourelis, H. Wang, F. Coccetti, G. Papaioannou, P. Pons and R. Plana (2010b), " Assessment of dielectric charging in electrostatically driven MEMS devices: A comparison of available characterization techniques," *J. Microelectron. Reliab.* **50**, 1615-1620.
- Zaghloul, U., F. Coccetti, G. Papaioannou, P. Pons and R. Plana (2010c), "A novel low cost failure analysis technique for dielectric charging phenomenon in electrostatically actuated MEMS devices," *2010 IEEE Int. Reliability Physics Symp.*, pp. 237-245, IEEE, New York.
- Zaghloul, U., B. Bhushan, P. Pons, G. Papaioannou, F. Coccetti and R. Plana (2011a), "On the Influence of Environment Gases, Relative Humidity and Gas Purification on Dielectric Charging/Discharging processes in Electrostatically Driven MEMS/NEMS Devices," *J. Nanotechnology* **22**, Art.# 035705.
- Zaghloul, U., G.J. Papaioannou, H. Wang, B. Bhushan, F. Coccetti, P. Pons, and R. Plana (2011b), "Nanoscale characterization of the dielectric charging phenomenon in PECVD silicon nitride thin films with various interfacial structures based on Kelvin probe force microscopy," *Nanotechnology* **22**, Art.# 205708.
- Zaghloul, U., B. Bhushan, P. Pons, G.J. Papaioannou, F. Coccetti, and R. Plana (2011c), "Nanoscale characterization of different stiction mechanisms in electrostatically driven MEMS devices based on adhesion and friction measurements," *J. Colloid and Interface Science* **358**, 1-13.
- Zaghloul, U., G. Papaioannou, B. Bhushan, F. Coccetti, P. Pons, and R. Plana (2011d), "Kelvin probe force microscopy based characterization techniques applied for electrostatic MEMS and thin dielectric films to investigate the dielectric charging phenomenon," *J. Vacuum Science and Technology (in press)*.
- Ziegler, D., N. Naujoks, and A. Stemmer (2008), "Feed-forward compensation of surface potential in atomic force microscopy ," *Rev. Sci. Instrum.* **79**, Art. #063704.

**Table 1** : Quantification of atomic concentration by XPS (% at) for **films SiN<sub>x</sub>** (source RX Mg, Ep=20 eV, correction Scofield)

SiH <sub>4</sub> / NH <sub>3</sub> gas ratio, r (sccm)	Power (W)	Temperature (°C )	C at%	O at%	N at%	Si at%	N/Si
0.15	20	200	-	1.8	45	53.2	0.845
0.25	20	200	-	0.6	44.6	54.8	0.813
0.6	20	200	-	2.5	38.5	59.0	0.653
0.8	20	200	-	2.4	37.9	59.7	0.635
0.45	40	200	-	1.4	40.2	58.4	0.688
0.45	60	200	-	1.55	40.5	57.95	0.698
0.45	80	200	-	1.0	41.1	57.8	0.711
0.45	100	200	-	1.5	41.5	57	0.728
0.45	20	250	-	1.6	40.1	58.3	0.687
0.45	20	300	-	0.8	40.2	59.0	0.681
0.45 (reference)	20	200	-	-	41	59	0.694

**Table 2:** PECVD deposition conditions for the reference SiN<sub>x</sub> sample (SiH<sub>4</sub>/NH<sub>3</sub> ratio = 0.45).

Parameter		Value
Gas flow rate (sccm)	SiH <sub>4</sub>	18
	NH <sub>3</sub>	40
	N <sub>2</sub>	1200
Radio frequency (RF) power (W)		20
Chamber pressure (mTorr)		1000
Radio frequency mode		13.56 MHz
Substrate temperature (°C)		200

## Figure Captions

Figure 1. The layer structure of the investigated samples and the dielectric charging assessment using the KPFM-based methodology: (a) charge injection in tapping mode over the dielectric surface, and (b) the resulting surface potential profile represented by  $U_s$  and FWHM.

Figure 2. An example KPFM surface potential maps obtained at different time points directly after the charge injection step using different pulse amplitude,  $U_p$ , for (a) positive, (b) negative voltage, and (c) the extracted potential profiles for  $\text{SiN}_x$  samples deposited using different gas ratio,  $r$ .

Figure 3. Dielectric charging characterization using the FDC measurements. (a) An example of a force-distance curve for the investigated  $\text{SiN}_x$  samples; (b) the retract data for force-distance curve obtained while different voltage is applied between the AFM tip and the sample; (c) a sample of the obtained adhesive force maps for a charged  $\text{SiN}_x$  film.

Figure 4. The time evolution of the measured KPFM surface potential represented by (a) surface potential amplitude,  $U_s$ , (b) potential distribution, FWHM, (c) absolute potential profile integral, and (d) normalized potential profile integral. The difference between KPFM decay (open symbols) and natural decay (solid symbols) is also highlighted in the figure.

Figure 5. An example of adhesive force decay with time measured using the FDC technique for the same  $\text{SiN}_x$  sample presented in **Fig. 4**: (a) adhesive force decay for charges which have been injected at 40 V, and (b) normalized adhesive force decay (open symbols) for injected charges under different voltage, and the corresponding values of KPFM potential profile integral (solid symbols).

Figure 6. The influence of the reactive gas ratio,  $r$ , on the charging (left) and discharging (right) processes as extracted from the KPFM measurements for charges which have been injected using different pulse amplitude: (a) surface potential amplitude,  $U_s$ , (b) potential distribution, FWHM, (c) potential profile integral for positive and negative charge injection, (d) a sample of  $U_s$  decay

with time for injected charges using the same pulse amplitude,  $U_p$ , (e) the decay time constant, and (f) stretch factor calculated from fitting.

Figure 7. The impact of reactive gas ratio,  $r$ , on the charging (left) and discharging (right) processes as measured from the FDC measurements for charges which have been injected using different voltage: (a) measured surface potential, (b) adhesive force, (c) an example of adhesive force decay with time for charges injected using same voltage, and (d) the calculated decay time constant from adhesive force time evolution.

Figure 8. FT-IR and XPS data for  $\text{SiN}_x$  films deposited using different gas ratio,  $r$ : (a) FT-IR spectra at an angle of  $70^\circ$ , and (b) N/ Si atomic ratio obtained from XPS analysis and the relative intensity Si-H (around  $2157 \text{ cm}^{-1}$  at  $70^\circ$ ,  $2160 \text{ cm}^{-1}$  at  $20^\circ$ ) versus N-H (around  $3348 \text{ cm}^{-1}$  at  $70^\circ$ ,  $3350 \text{ cm}^{-1}$  at  $20^\circ$ ) from FT-IR.

Figure 9. The effect of RF power on the charging (left) and discharging (right) processes as extracted from the KPFM measurements for charges which have been injected using different pulse amplitude: (a) surface potential amplitude,  $U_s$ , (b) potential distribution, FWHM, (c) potential profile integral for positive and negative charge injection, (d) a sample of  $U_s$  decay with time for injected charges using the same pulse amplitude,  $U_p$ , (e) the decay time constant, and (f) stretch factor calculated from fitting.

Figure 10. The influence of deposition RF power on the charging (left) and discharging (right) processes as measured from the FDC measurements for charges which have been injected using different voltage: (a) measured surface potential, (b) adhesive force, (c) an example of adhesive force decay with time for charges injected using same voltage, and (d) the calculated decay time constant from adhesive force time evolution.

Figure 11. FT-IR and XPS data for  $\text{SiN}_x$  films deposited using different RF power: (a) FT-IR spectra for  $\text{SiN}_x$  films deposited using different RF power at an angle of  $70^\circ$ , and (b) N/ Si atomic ratio obtained from XPS analysis and the relative intensity Si-H (around  $2157 \text{ cm}^{-1}$  at  $70^\circ$ ,  $2160 \text{ cm}^{-1}$  at  $20^\circ$ ) versus N-H (around  $3348 \text{ cm}^{-1}$  at  $70^\circ$ ,  $3350 \text{ cm}^{-1}$  at  $20^\circ$ ) from FT-IR.

Figure 12. The effect of substrate temperature on the charging (left) and discharging (right) processes as extracted from the KPFM measurements for charges which have been injected using different pulse amplitude: (a) surface potential amplitude,  $U_s$ , (b) potential distribution, FWHM, (c) potential profile integral for positive and negative charge injection, (d) a sample of  $U_s$  decay with time for injected charges using the same pulse amplitude,  $U_p$ , (e) the decay time constant, and (f) stretch factor calculated from fitting.

Figure 13. The influence of substrate temperature on the charging (left) and discharging (right) processes as measured from the FDC measurements for charges which have been injected using different voltage: (a) measured surface potential, (b) adhesive force, (c) an example of adhesive force decay with time for charges injected using same voltage, and (d) the calculated decay time constant from adhesive force time evolution.

Figure 14. FT-IR and XPS data for  $\text{SiN}_x$  films deposited using different substrate temperature: (a) FT-IR spectra for  $\text{SiN}_x$  films deposited using different substrate temperature at an angle of  $70^\circ$ , and (b) N/ Si atomic ratio obtained from XPS analysis and the relative intensity Si-H (around  $2157 \text{ cm}^{-1}$  at  $70^\circ$ ,  $2160 \text{ cm}^{-1}$  at  $20^\circ$ ) versus N-H (around  $3348 \text{ cm}^{-1}$  at  $70^\circ$ ,  $3350 \text{ cm}^{-1}$  at  $20^\circ$ ) from FT-IR.

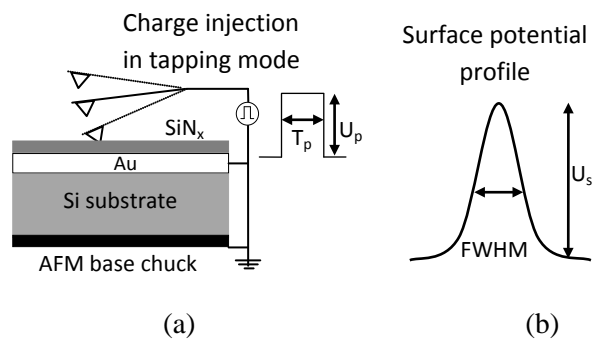


Fig. 1

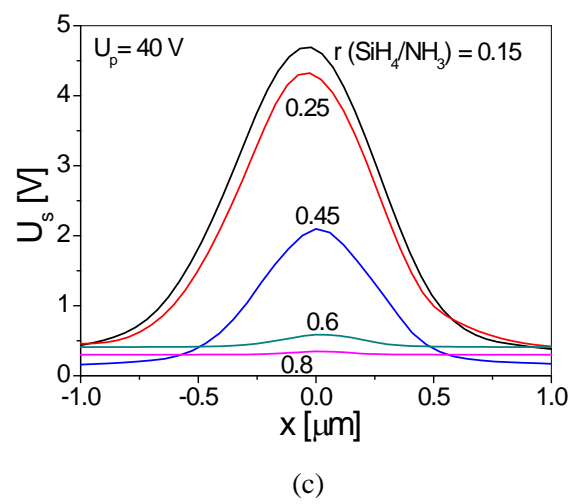
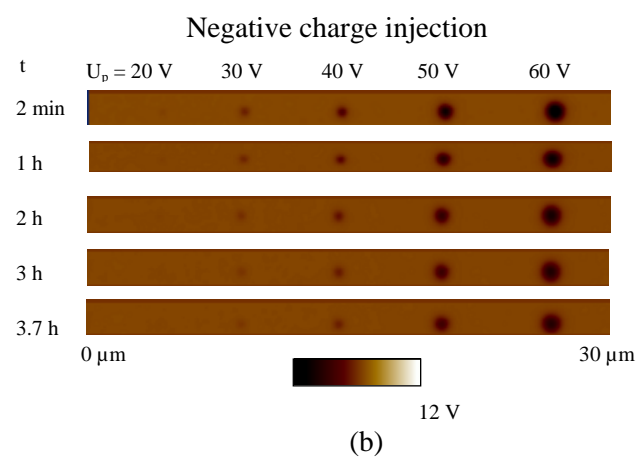
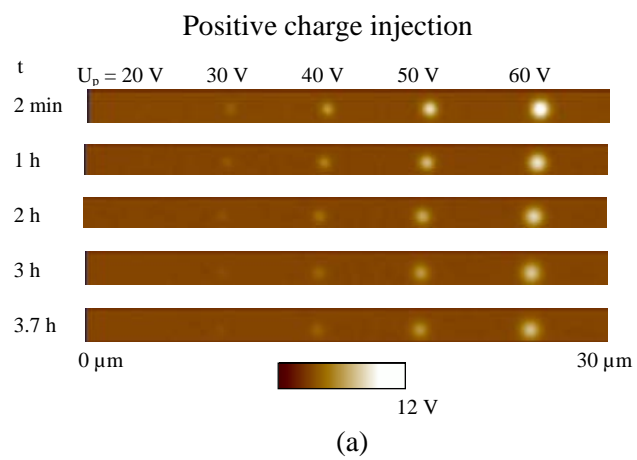
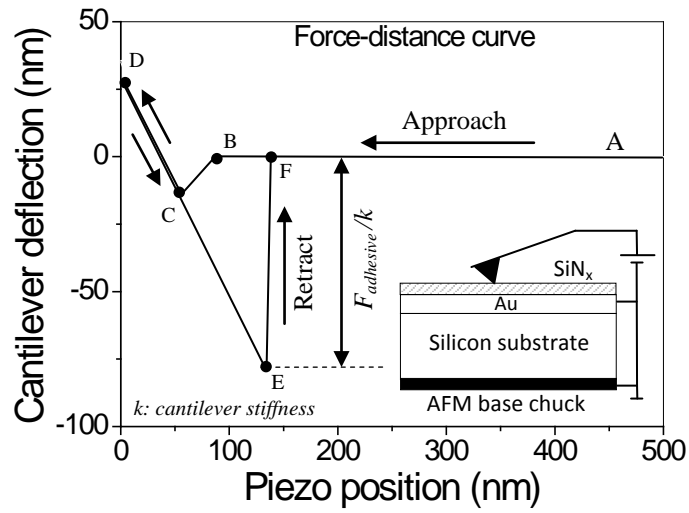
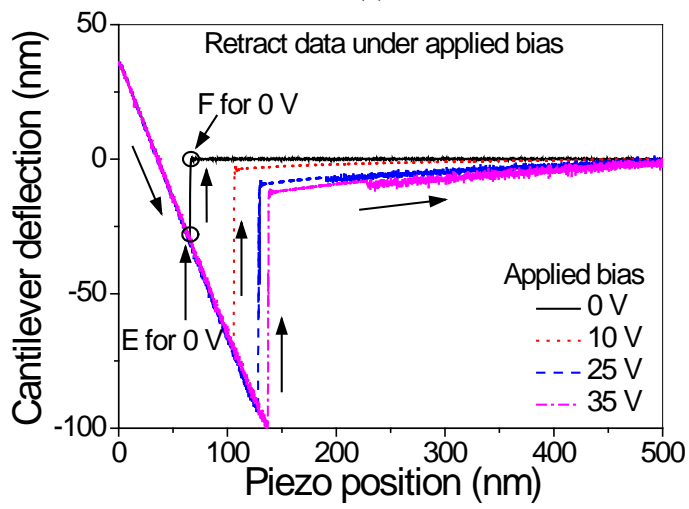


Fig 2

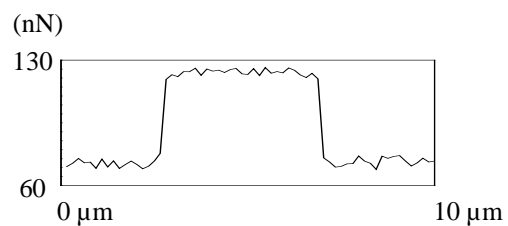
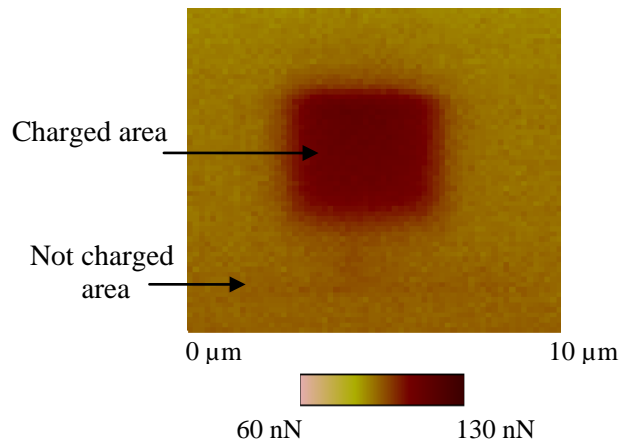


(a)



(b)

Adhesive force map for a charged SiN<sub>x</sub>



(c)

Fig. 3

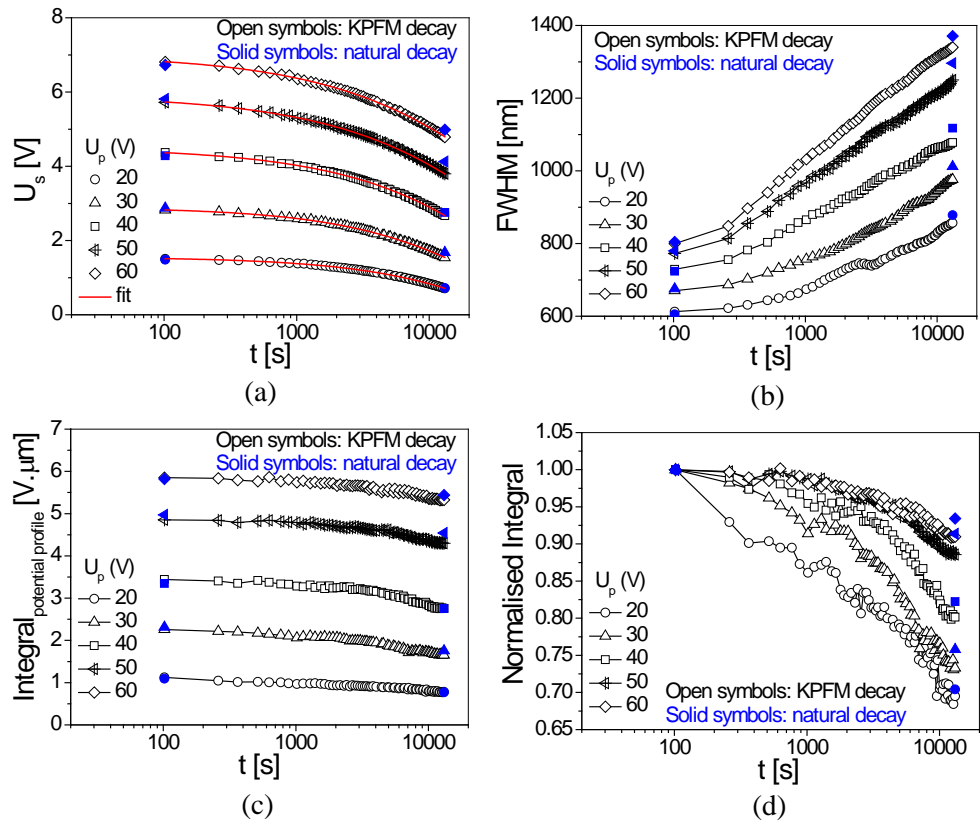
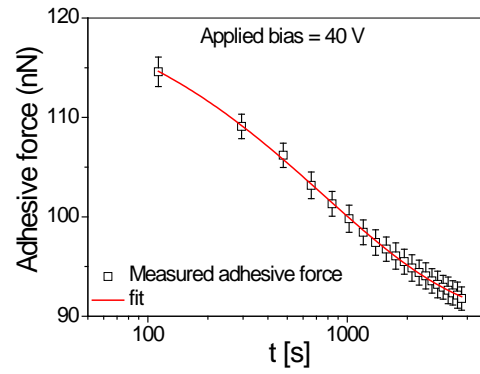
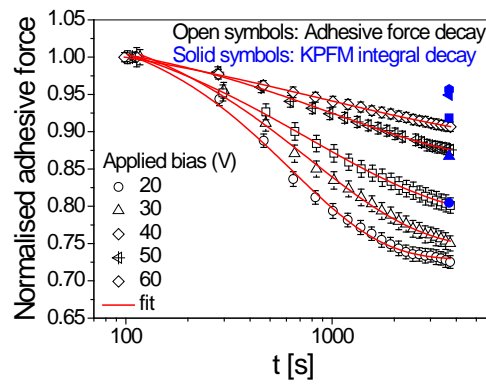


Fig 4



(a)



(b)

Fig. 5

Influence of gas ratio ( $\text{SiH}_4/\text{NH}_3$ ) based on KPFM measurements

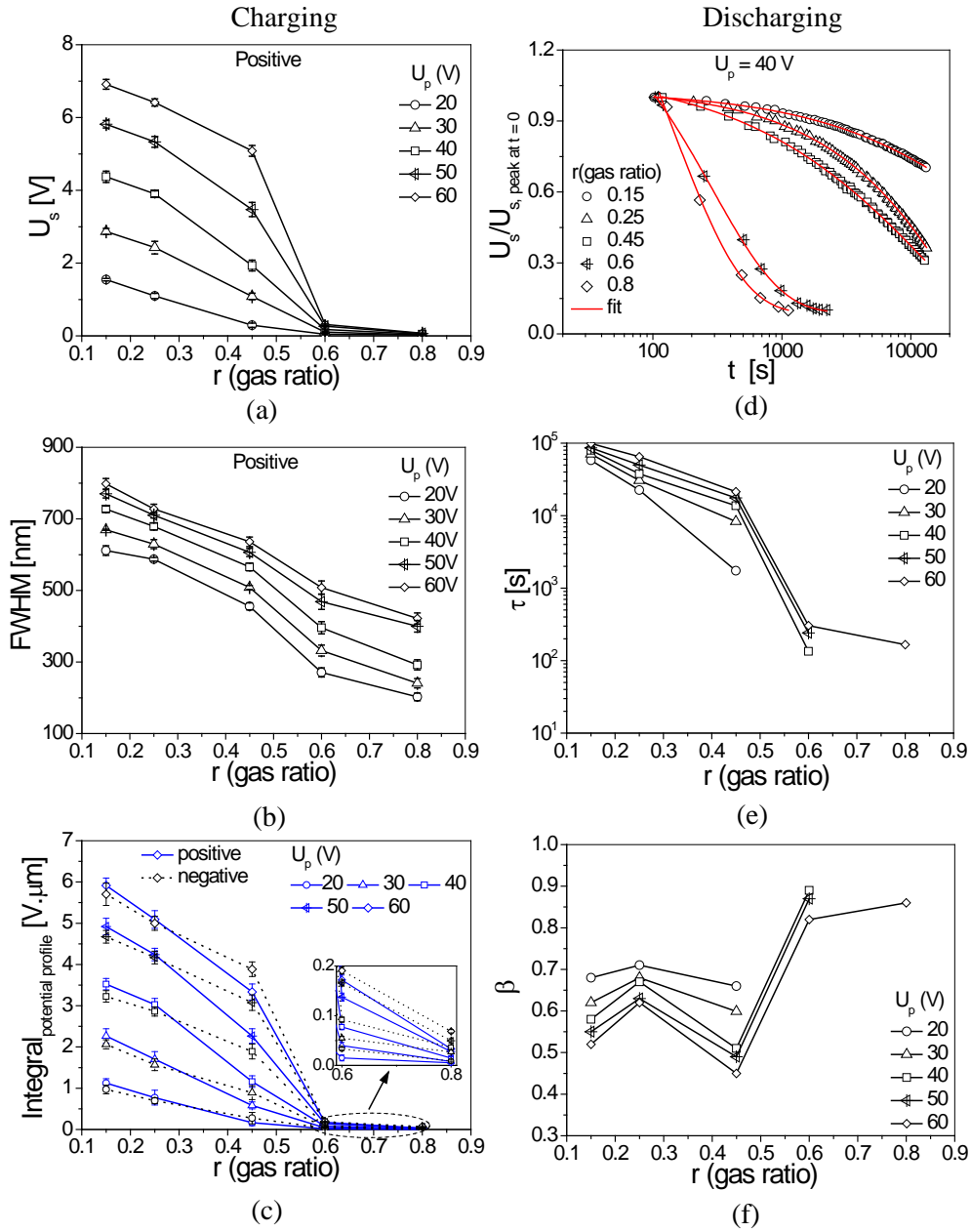


Fig 6

Influence of gas ratio ( $\text{SiH}_4/\text{NH}_3$ ) based on FDC measurements

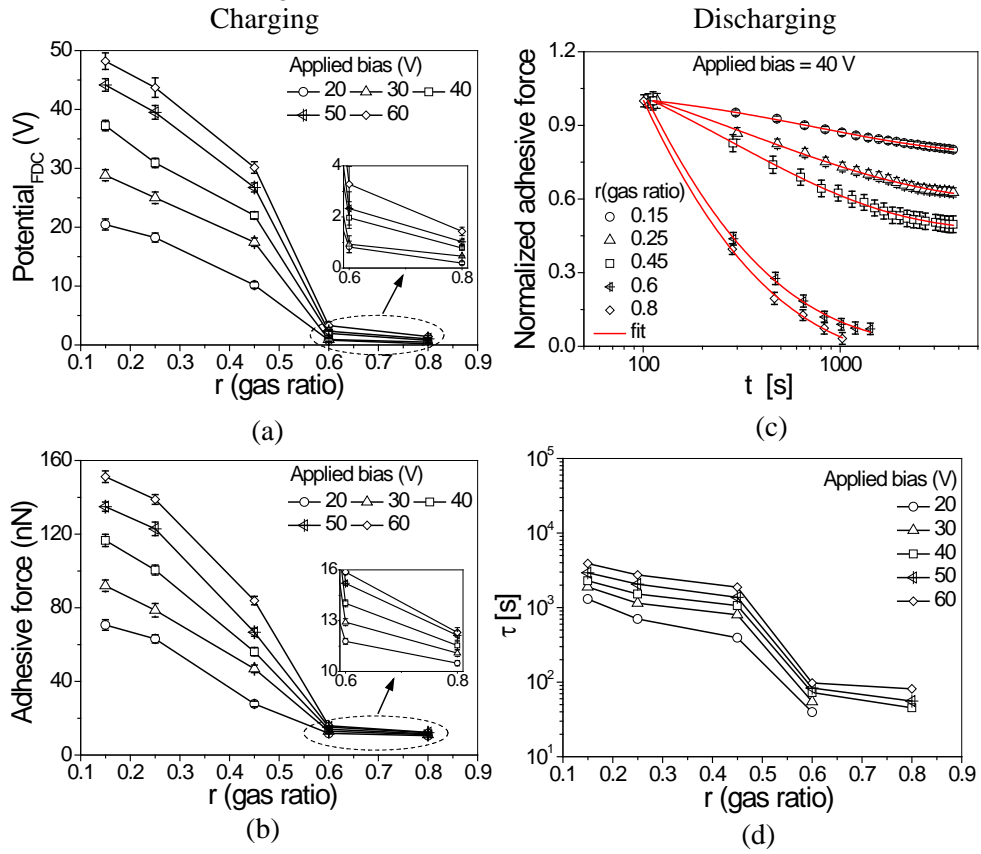
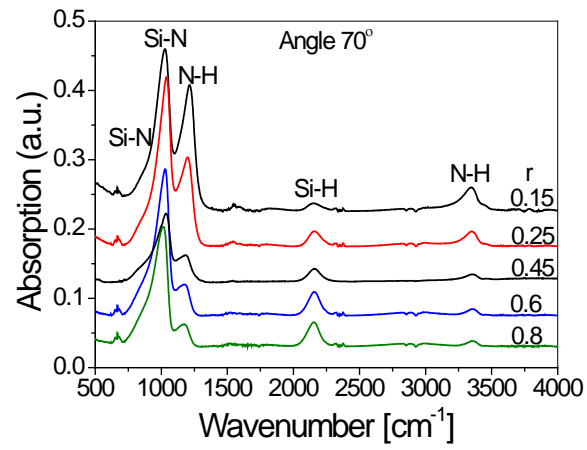
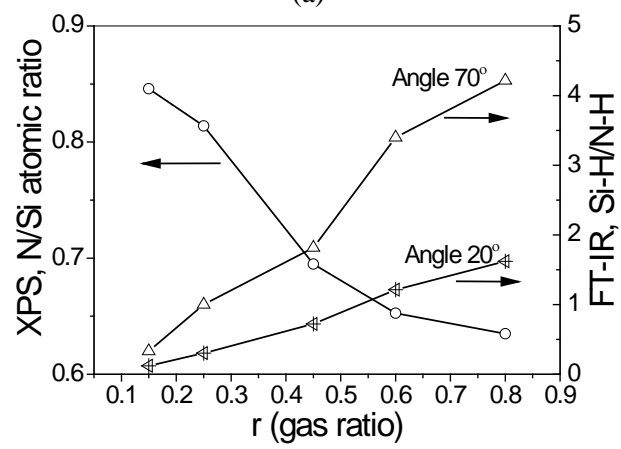


Fig 7



(a)



(b)

Fig. 8

Influence of deposition RF power based on KPFM measurements

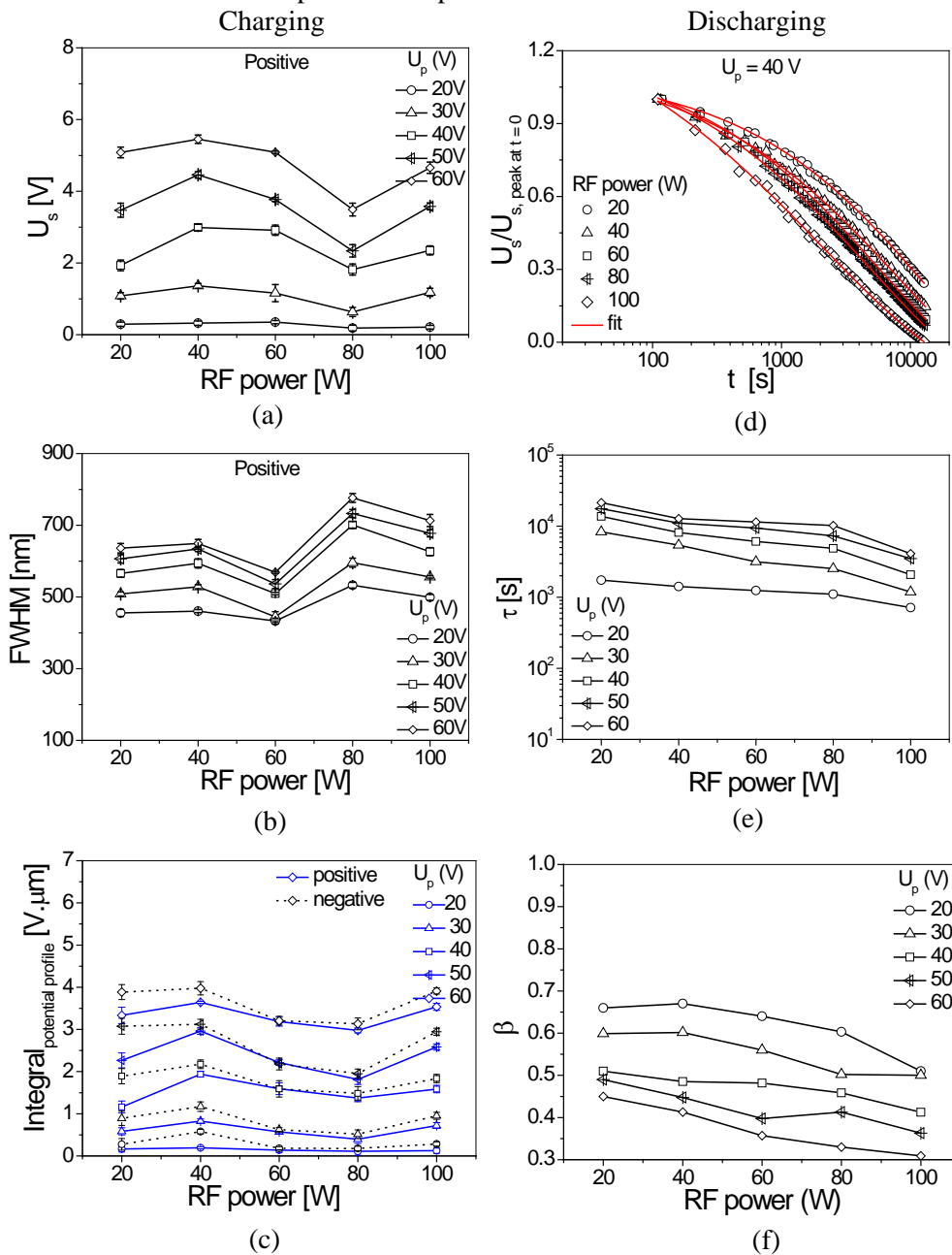


Fig 9 c) add a horizontal line ?

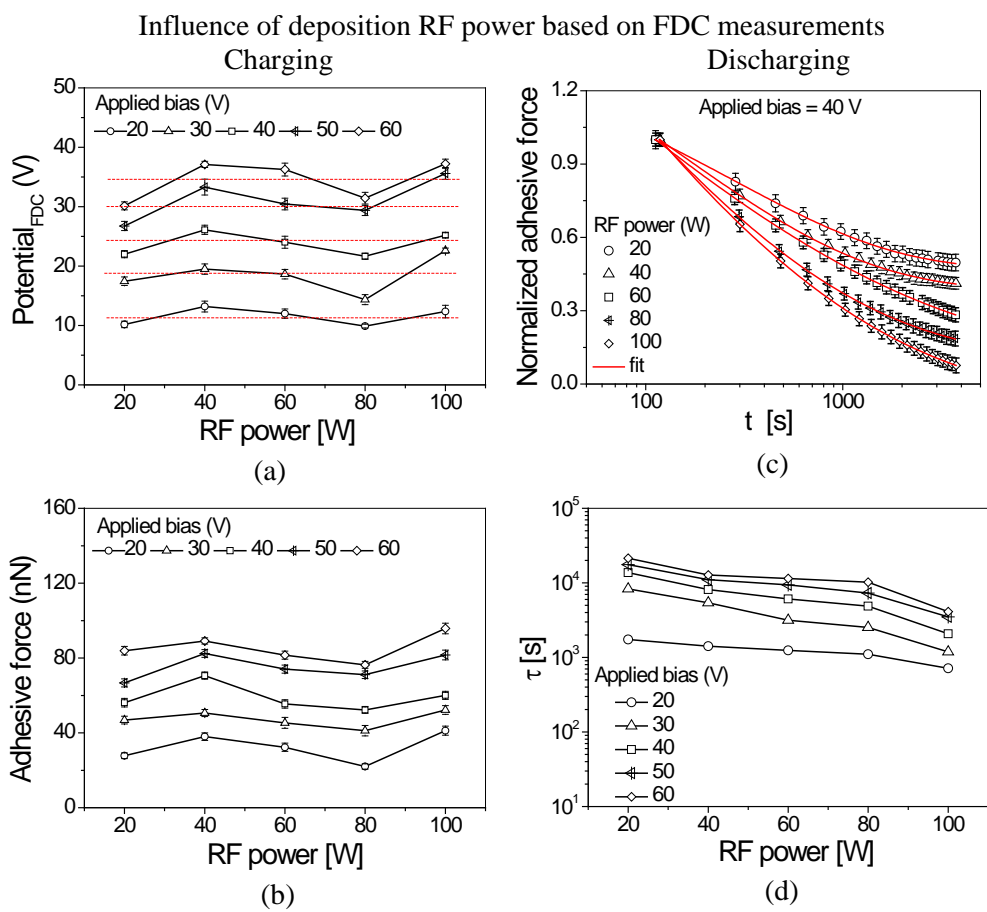
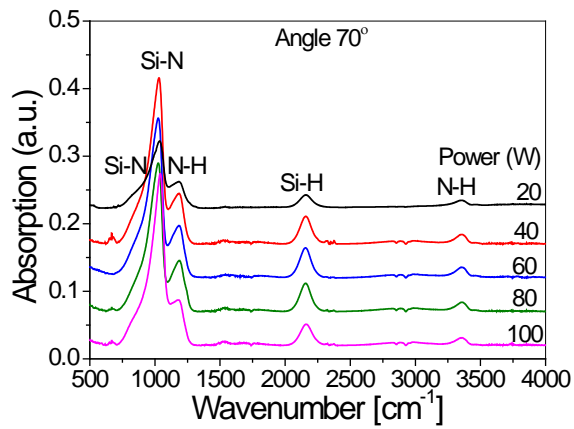
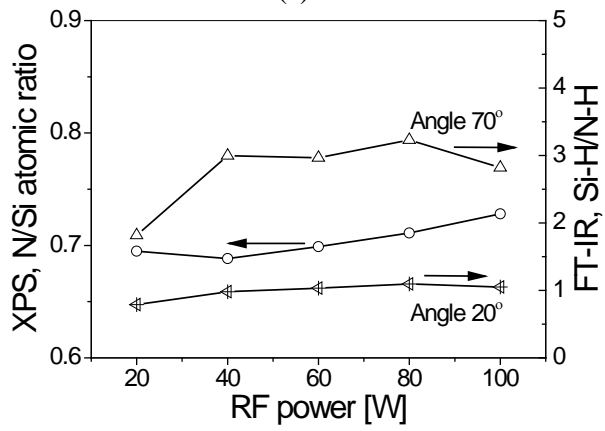


Fig 10



(a)



(b)

Fig. 11:

Influence of substrate temperature based on KPFM measurements

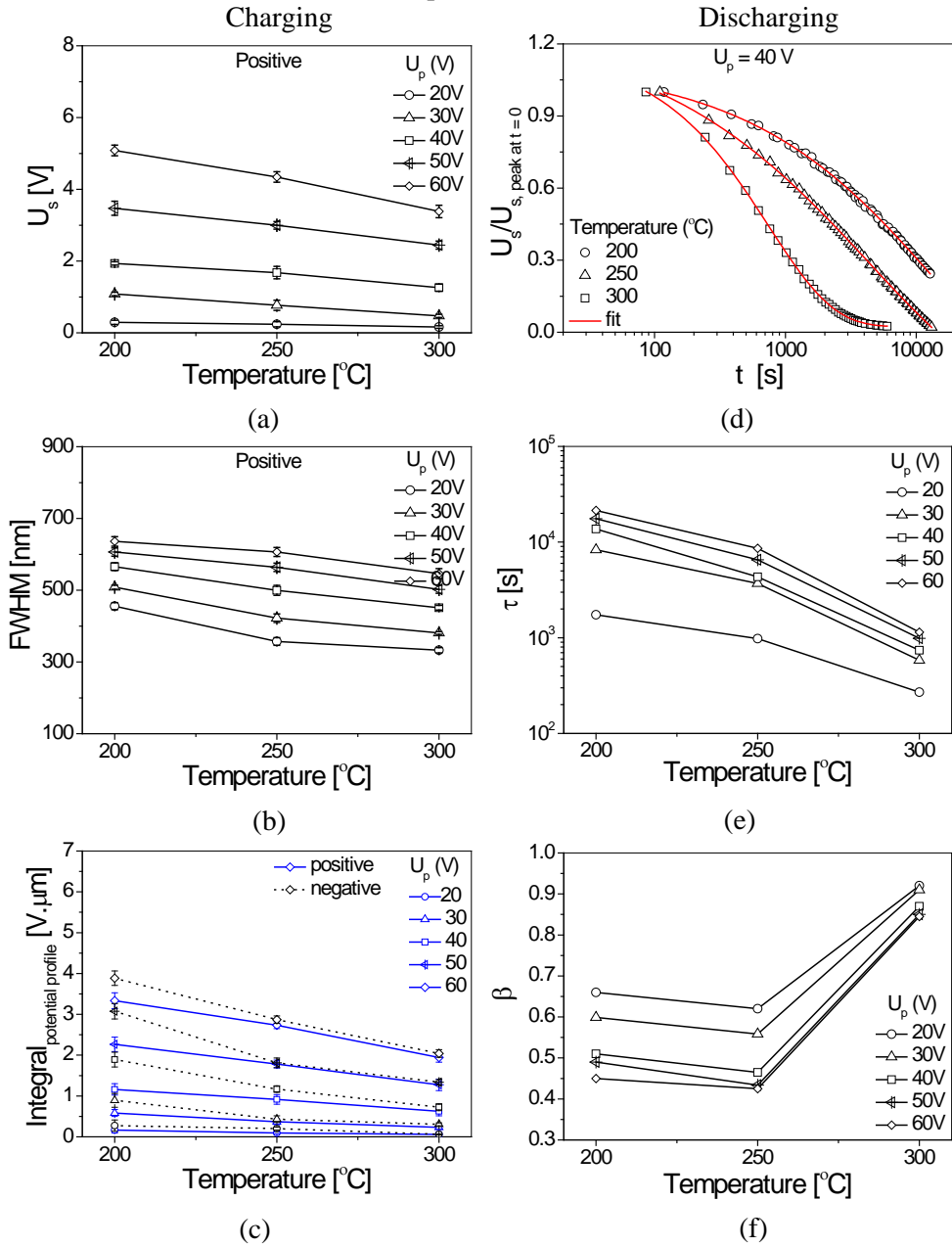


Fig 12

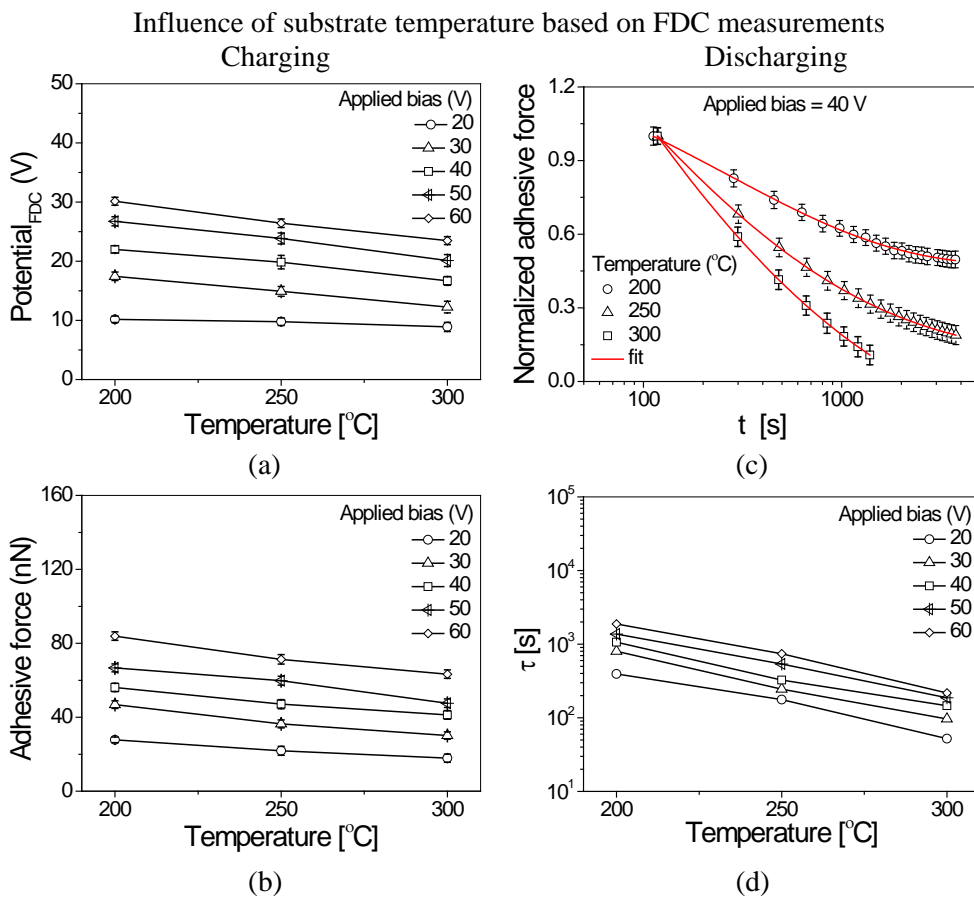
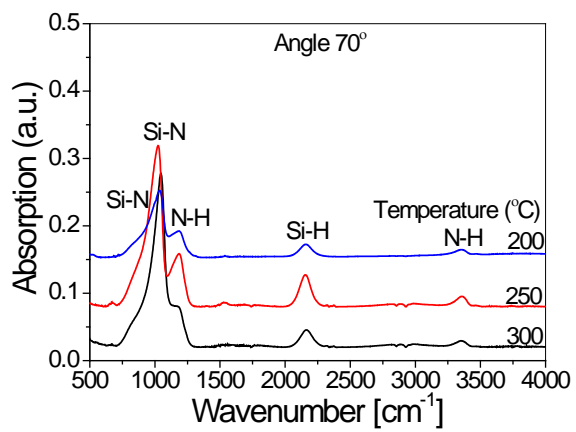
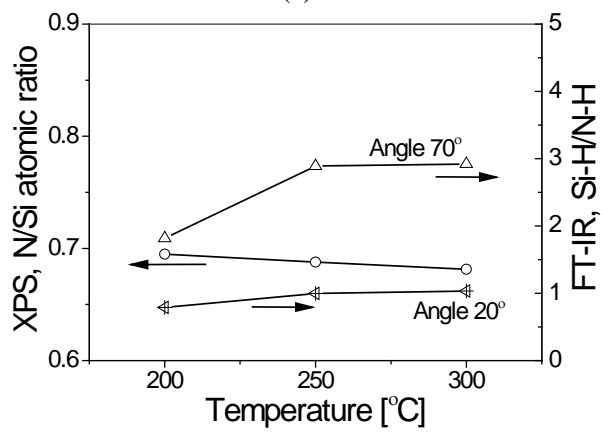


Fig 13



(a)



(b)

Fig 14